# Electric-Discharge-Mediated Jetting, Crowning, Bursting, and Atomization of a Droplet

Bhaskarjyoti Sarma,[1] Sunny Kumar,[2] Amaresh Dalal,[1] Dipankar N. Basu,[1] and Dipankar Bandyopadhyay[2,3,*]

[1] *Department of Mechanical Engineering, Indian Institute of Technology Guwahati, Assam 781039, India*
[2] *Department of Chemical Engineering, Indian Institute of Technology Guwahati, Assam 781039, India*
[3] *Centre for Nanotechnology, Indian Institute of Technology Guwahati, Assam 781039, India*

(Received 30 August 2020; revised 8 November 2020; accepted 16 November 2020; published 6 January 2021)

We observe bursting, crown or jet formation, and atomization phenomena when electric discharge is confined at the base of a liquid droplet. Emulating an electrowetting-on-dielectric setup, a hemispherical droplet is placed on a cathode-isolator platform while a pointed anode from the top stimulates the discharge inside the drop. Beyond a critical intensity of the applied electric field, the dielectric layer under the droplet suffers breakdown to generate the discharge. Within a few milliseconds, the electric discharge stimulates crown or jet formation or bursting of the droplet. A lower (higher) salt loading in the droplet at lower (higher) field intensity leads to the jetting (bursting). The crown formation happens only for an intermediate window of salt loadings and electric field intensities. The energy conversion efficiency is found to be approximately 25%–30% for droplet bursting while the same is less than 2% for jet or crown formation. The experiments and simulations uncover that the location of the pointed electrode in the droplet and the separation distance of electrodes can be some crucial factors in varying the location of discharge, which eventually leads to the aforementioned flow morphologies. Further, the interplay between surface tension, viscous, and electric field forces inside the droplet is found to play crucial roles to engender the flow patterns. The setup transiently shows up the formation of end pinching of jets, microjets, high-aspect-ratio liquid threads, upward moving jet, liquid spikes riding on a crown rim, and capillary breakup of jets. Such electric-discharge-mediated droplet disintegration resembles closely the previously reported laser or plasma-induced phenomena. Further, with proper tuning of the aforementioned control parameters, the proposed methodology is expected to find its application in several cutting-edge technologies, such as inkjet printing, tissue ablation, or electroporation etc.

DOI: 10.1103/PhysRevApplied.15.014005

## I. INTRODUCTION

Electric field discharge during lightning [1] or generation of the electric arc at the contact of a charged insulator with a conductor [2] has been among the very intriguing natural phenomena that fascinated researchers for ages. Over the years, a great deal of attention has been given to comprehend such phenomena because they can be useful in various applications such as triboelectric energy harvesting [3], mixing [4,5], gas-discharge lamps, or ionizing tubes [6], among others. Interestingly, confining an electric discharge inside a microfluidic system may convert the electrical energy into the mechanical one to emerge a number of fascinating fluid dynamical phenomena such as splashing, crowning, jetting, or bursting. Along similar lines, of late, extensive research activities have been observed in exploring the physics associated with the deformation and disintegration of droplets with the help of various external fields, such as electric, magnetic, or laser excitations [7–9].

Studies on the splashing, crowning, jetting, or bursting of fluids started a long time ago [10–12]. For example, the pioneering contributions from Worthington [13] have uncovered the possible flow morphologies assumed by an impacting liquid droplet on a solid surface. Later, the jetting or splashing during the impact of a liquid or solid object on a fluid medium was found to accompany the formation of crown or umbrella flow morphologies [11,14,15]. Subsequently, in recent years, with the development of characterization facilities [16], the physics associated with the formation of a jet, crown [11,17,18], or fragmentation of a droplet [19] have been extensively explored. In the present era of microscale devices, the fragmentation of the droplets, jets, or crowns into the miniaturized forms have shown their relevance in enhancing mass, momentum, and heat transport [20,21].

*dipban@iitg.ac.in

 

Such explorations have contributed significantly to the development of cutting-edge applications, such as superhydrophobic surfaces [22], droplet microfluidics [23], spray painting, atomization of propellants [24], nebulizers, sprinklers [25], distributors [26], and inkjet printing [27].

However, the field-induced splashing, crowning, jetting, or bursting are found to be very different from the similar phenomena observed during the impact of an object on a liquid surface. In this direction, recently, such phenomena have been explored under the influence of various external triggers such as electric field [28], photonic excitations [8], thermal gradient [29], or shock waves [30]. For example, the expansion and collapse of a vapor bubble produced by an electric spark in an electrolyte solution are found to generate a pulsed liquid microjet of 30 $\mu$m diameter having a peak velocity of 90 m/s, aiming its use as an intravascular injection during microsurgeries [31]. Similarly, the cavitation bubbles generated during electric discharge inside a macroscopic droplet in a microgravity environment have been found to induce jetting and splash [28]. Again, Karri *et al.* [32] showed that an oscillating and collapsing cavitation bubble positioned near a liquid surface and coaxially to a cylindrical hole engenders jetting and sprays via breakup of the jets. In fact, the advancement in the imaging techniques has enabled a more effective characterization of these events of drop shaping or drop breakup to the jet, crown, and atomized droplets with the use of laser pulse or x-ray pulse [33–35]. The miniaturization of the droplets during laser-induced breakdown spectroscopy (LIBS) [36], lithography [37] or laser ablation [38] is among the commercial processes that already exist.

Fundamentally, the origin of diverse flow morphologies during the drop impact, splashing, or breakup can be attributed to various factors, which include the surface and bulk properties of the impacting object [18,39], velocity and angle of attack of the impacting object [40], and the texture and roughness of the surface on which the impact takes place [41]. Despite their diversified origin, the crowns or jets are ejected during the impact of a solid or liquid object in a bulk fluid as a consequence of a very large axial pressure gradient created at the crown or jet base [33,42,43]. For example, the transfer of the inertial force of the impacting droplet in the liquid medium is the primary reason for the formation of axial columnar jets on a deformable liquid-air interface [11,44]. The progress in the domains of stability analysis [45,46] and computational fluid dynamics [40,47] in the past few decades have also helped in unfurling several critical aspects of flow dynamics associated with crown formation, crown sealing, buckling, ejecta-sheet formation, or pinchoff.

In view of this background, we uncover that confining an electric discharge inside a sessile droplet can be one of the very simple but interesting ways for splashing, crowning, jetting, or fragmentation of the same. The experiments are performed in a setup resembling the electrowetting-on-dielectric (EWOD) setup [48,49] in which a droplet has been placed on an electrode-isolator pair while a pointed electrode is inserted into the drop from the top to confine the discharge inside the droplet, as schematically shown in Fig. 1(a). A series of experiments are performed to identify the pathways to control the location of the electric field discharge by tuning the electrode distance, the magnitude of the externally applied electric field, viscosity, electrical conductivity, and surface tension of the droplet. Both the experiments and simulations uncover that the location of the pointed anode in the droplet, alongside the separation distance of electrode from the base of the droplet, can be some crucial factors in varying the location of discharge, which eventually leads to the metastable liquid jets, crowns, microthreads, or microdroplets. The roles of the electric field, inertial, viscous, and surface tension forces in predicting the experimentally measured time scales along with the energy conversion efficiencies of the different processes are also reported. The proposed methodology can be employed as an alternative technique to disintegrate the macroscopic droplets into the microscopic ones for improved heat, momentum, and mass transport in various microfluidic applications, including, but not limited to, inkjet printing [27], electrospraying [50], tissue ablation [51], or electroporation [52], etc. The potential of the proposed method is highlighted through comparison with some of the existing methods of liquid-jet formation, atomization separately in Sec. III H (see also Sec. SI within the Supplemental Material [53]).

The paper is organized as follows: in Sec. II, we briefly discuss the materials used and their properties, experimental setup, and various experimental procedures; in Sec. III, the results obtained from experiments and simulations are discussed and analyzed before summarizing the salient features in the Sec. IV.

## II. EXPERIMENTAL METHOD AND MATERIALS

### A. Experimental procedure

The experimental procedure is schematically shown in Fig. 1(a). In this setup, with the help of a micropipette, a 5-$\mu$l droplet is placed on a polydimethylsiloxane- (PDMS, Dow Corning, India, SYLGARD 184 kit) coated indium-tin-oxide (ITO) glass surface (MG Super Lab, dimension: 12.5 $\times$12.5 $\times$ 1.1 mm$^3$). The PDMS layer acted as the dielectric isolator between the ITO cathode and conducting droplet, while the glass layer acted as a bottom isolator, as shown in Fig. 1(b). The droplet is connected to the electric field with the help of a platinum (Pt) wire anode (dia. 150 $\mu$m, Surgeon Sons, India) from the top, as shown in Figs. 1(a) and 1(c). The electrodes are connected to a dc power source (SES Instruments Pvt. Ltd., range: 0–1500 V) to generate the electric field ($\Psi$) across the electrodes placed at a distance $h_e$ apart. Here, we directly

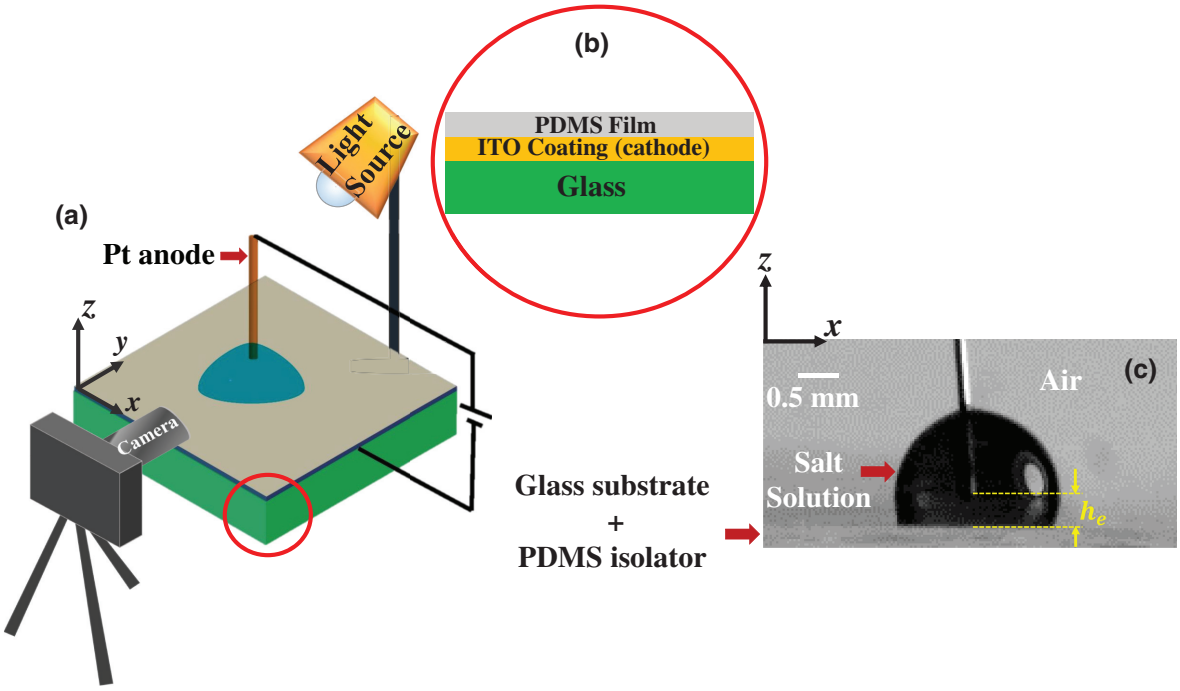


FIG. 1. Schematic diagram of the experimental setup. Image (a) shows an isometric view where a droplet is dispensed upon a thin PDMS film coated on an ITO-glass substrate. A pointed Pt wire connected from the top of the droplet acts as the anode. The different layers of the isolator-cathode-isolator substrate composed of PDMS-ITO-glass are shown as the inset in the image (b). Image (c) shows the photographic side view of an experiment from which the position of the droplet and Pt anode can be visualized. The notation $h_e$ indicates the distance between the droplet base and anode. The spatiotemporal evolution of the concerned hydrodynamic features has been followed by a high-speed camera, and illumination is provided by a light source positioned opposite to the camera.

supply a high voltage to the electrodes instead of slowly ramping of voltage. Notably, along with the applied potential ($\psi$), the location of the anode is another critical parameter affecting the strength of the discharge as well as the ensuing hydrodynamics. The gap between the anode and dielectric is maintained with the help of a vertically moving platform, thereby generating an electric field of desired intensity. In addition, to maintain symmetry, special care has to be taken to place the electrode near the central portion of the droplet with respect to the horizontal $X$-$Y$ plane, as shown in Fig. 1(a). The repeatability of the results under varied conditions confirm the robustness of the proposed experimental setup (refer to Sec. SII and SIII within the Supplemental Material [53]). It may be noted here that the Pt anode is cleaned after each experiment to enhance the repeatability of the results. Further, in order to control the variations in the initial volume ($V_{\text{drop}}$) of the dispensed droplets, the microtips attached to the micropipette are replaced after dispensing every drop. The dynamics of atomization are captured with a high-speed camera for subsequent analysis, as discussed in Sec. II D. Unless stated otherwise, the electric discharge is generated across a 5-$\mu$l droplet of electrical conductivity 13.18 mS/cm with the help of a 500-V electric field potential applied through the electrodes.

### B. Dielectric substrate preparation

The PDMS film is spin coated on the ITO glass to prepare the isolator-cathode-isolator (PDMS-ITO-glass) base substrate, as shown in Fig. 1(b). For this purpose, initially, the ITO-coated glass slides are cleaned following the standard procedure, as described in Sec. SIV within the Supplemental Material [53]. Simultaneously, the prepolymer is prepared by mixing the PDMS (properties in Table I) and the curing agent in the weight ratio of 10:1 before degassing the mixture. The resulting solution is then mixed with hexane (analytical grade, Sigma-Aldrich) in the ratio of 110:10:1. Following this, the solution is spin casted with the help of a spin coater (SPINNXG - P1, Apex India Pvt. Ltd.) on the ITO-coated glass substrate. Thereafter, the films are cured overnight at 100°C in the

TABLE I. Properties of deionized (DI) water and PDMS [54].

| Liquid | DI-water | PDMS |
|---|---|---|
| Density ($\rho$, kg/m$^3$) | 997.05 | 970 |
| Viscosity ($\eta$, mPa s) | 0.890 | 3500 |
| Conductivity ($\sigma_s$, mS/cm) | $5.6 \times 10^{-5}$ | $2.5 \times 10^{-13}$ |
| Surface tension ($\gamma$, mN/m) | 72.1 | 21 |
| Dielectric Constant ($\epsilon$) | 80.0 | 2.65 |

vacuum oven (Spac-N-Service Pvt. Ltd., India). Spin coating at 2500 rpm with an acceleration of 5 m/s$^2$ and duration of 120 s led to a PDMS film of thickness, $h \sim 1(\pm 0.1)\ \mu$m, on the ITO glass [55]. The thickness of the films and the surface roughness are measured with the help of a surface profilometer (Dektak 150 surface profiler, Veeco Instruments Inc.) and atomic force microscopy (Bruker, Innova), respectively. The transparent dielectric films thus prepared have a surface roughness in the nanometer range, almost $2 \pm 0.5$ nm. The hydrophobic nature of the surfaces is confirmed by measuring the equilibrium contact angle, $\theta_{eq}$ (refer to Supporting Table II in Sec. SV within the Supplemental Material [53]), of DI-water droplets in a goniometer (Apex India). The dielectric substrates are preserved in the vacuum desiccators, if not used immediately in experiments.

### C. Droplet preparation

Different types of fluids are used to prepare the droplets for the experiments, as listed in Table II. The base fluid is chosen to be the DI water (Merck Millipore, grade I, resistivity 18.2 MΩ cm at 25°C) and the physical properties of the same are shown in Table I. The viscosity of the droplet is tuned by mixing glycerol (Merck, 98% pure), while the electrical conductivity of the droplet is varied by mixing KCl (Sisco Research Laboratories Pvt. Ltd., Mumbai) into the solutions. In order to prepare droplets of the glycerol-water mixture with a known electrical conductivity, salt solutions of glycerol and water are prepared separately beforehand and then mixed at different volumetric ratios, as per the requirement of the experiments. The concentrations of the salt solutions ($C_s$) for different samples are shown in Table II. The solutions are categorized as low ($\eta \leq 1$ mPa s), moderate (1 mPa s $< \eta \leq 10$ mPa s), and high viscosity ($\eta > 10$ mPa s), depending upon the volumetric ratio of glycerol and DI water present in the droplet. Table II enlists the values of viscosity, surface tension, density, and conductivity of the solutions used in the experiments. These are measured by using rheometer (PHYSICA MCR 101; Aanton Paar), tensiometer (DY-300; Kyowa), density meter (Aanton Paar; DMA 4500), and conductivity meter (Orion 3-star conductivity benchtop model, Thermo Scientific), respectively. The conductivity meter had been calibrated against the standard solution of 0.1 M KCl each time before the measurements are made.

### D. Imaging and experimental analysis

The dynamics of fast-paced atomization events are reordered using the high-speed videography technique, which is deemed more reliable than the conventional flash-photography methods. The dynamics of the droplet during and after the electric discharge are captured with a high-speed video camera (Photron, FASTCAM Mini UX100) fitted with a zoom lens (Navitar Macro zoom, 18–108 mm F/2.5) with a recording speed ranging from 4000 to 10000 frames per second (fps). The shutter speed employed is determined from the relation, shutter speed $\leq 1/\text{fps}$, to obtain images with better spatial and temporal resolutions. The shortest shutter speed employed is 80 $\mu$s while the phenomenon is captured at 10 000 fps. The frame speed and resolution are optimized based on the inherent time and length scales of each phenomenon reported. The background is continuously illuminated by a high-intensity light-emitting diode light (Phlox, 130000 lux), which enhanced the quality of the captured videos by boosting the contrast. The recordings are triggered manually and saved in a computer for subsequent analyses. Images are analyzed with the help of open-source software ImageJ [58].

## III. RESULTS AND DISCUSSION

The experimental setup, described previously in Sec. II A [refer to Fig. 1(a)], ensures the formation of a charging multilayer capacitor when a dc electric field is generated across the droplet with the help of the Pt anode and ITO cathode. The magnitude of the capacitance due

TABLE II. Composition and properties of the experimental solutions ([a][56], [b][57]).

| Solution | Composition ($C_s$) | Viscosity ($\eta$, mPa s) | Conductivity ($\sigma_s$, mS/cm) | Surface tension ($\gamma$, mN/m) | Density ($\rho$, kg/m$^3$) |
|---|---|---|---|---|---|
| 1 | 0.01 M KCl + DIW | 0.890[a] | 1.33 | 72.12[b] | 997.35[a] |
| 2 | 0.05 M KCl + DIW | 0.890[a] | 6.74 | 72.19[b] | 998.55[a] |
| 3 | 0.1 M KCl + DIW | 0.889[a] | 13.18 | 72.27[b] | 1000.41[a] |
| 4 | 0.5 M KCl + DIW | 0.887[a] | 64.20 | 72.96[b] | 1018.29[a] |
| 5 | 1.0 M KCl + DIW | 0.886[a] | 111.70 | 73.82[b] | 1041.25[a] |
| 6 | 0.1 M KCl + 50% Gly. + 50% DIW | 6.88 | 13.18 | 70.1 | 1128.7 |
| 7 | 0.1 M KCl + 65% Gly. + 35% DIW | 18.25 | 13.18 | 68.7 | 1168.3 |
| 8 | 0.1 M KCl + 70% Gly. + 30% DIW | 26.96 | 13.18 | 66.5 | 1181.5 |
| 9 | 0.1 M KCl + 80% Gly. + 20% DIW | 66.90 | 13.18 | 65.3 | 1207.9 |

[a]DIW = DI water. [b]Gly = Glycerol.

to the presence of the approximately 1-$\mu$m PDMS film is determined to be about $C = \epsilon_0\epsilon_p A/h = 5.28$ nF, where $\epsilon_0$, $\epsilon_p$, and $A$ denote the permittivity of free space, dielectric constant, and area of the PDMS film, respectively. In such a scenario, when the electric field intensity is increased beyond a threshold value ($\Psi \geq \Psi_{\text{cric}}$), the dielectric barrier of the PDMS film breaks down, leading to an electric field discharge through the droplet. This critical electric field, $\Psi_{\text{cric}}$, for this discharge is found out after performing a series of experiments, as discussed separately in Sec. III G 1. The electric discharge is facilitated by the submillimetric gap between the electrodes ($h_e \leq 1$ mm), while the electric potential ($\psi$) has been varied between 400–1200 V. Interestingly, the dielectric breakdown is analogous to the flash produced in the high-voltage electricity supply wires in the presence of water droplets (pollutants) due to the degradation of the electrical insulation [59,60]. The phenomenon is also comparable to the useful dielectric barrier discharges (DBDs), routinely used in the ozone generation, incoherent excimer ultraviolet sources, greenhouse gas recycling, and synthetic jet actuation [61,62].

The experimental parameters and thermophysical properties, which are highly relevant for the present experiments, are electric field potential ($\psi$), initial radius ($r_d$), surface tension ($\gamma$), density ($\rho$), and dynamic viscosity ($\eta$) of the droplet. These parameters can further be clubbed together to form the following set of nondimensional numbers: capillary number, $\text{Ca} = \eta U/\gamma$, Ohnesorge number, $\text{Oh} = \eta/\sqrt{\rho\gamma L}$, and electric field Bond number, $\text{Bo} = (\epsilon_0\epsilon_p r_d \Psi^2)/\gamma$. The Ca signifies the relative strength of the viscous over surface-tension force, Oh signifies the relative strength of the viscous force over the combined influence of inertial and surface-tension forces, and Bo signifies the dominance of the electric field force over the surface-tension force. In this study, the radius of the droplet, $r_d$, is considered as the characteristic length scale, $L$, whereas the maximum velocity of the corresponding hydrodynamic feature (namely, crown, jet, or bursting) has been considered as the characteristic velocity, $U$. The maximum velocity, $U$, has been estimated by considering the first few frames (roughly four) of the evolution of the respective hydrodynamic features, just after their emergence. Here, in all the experimental realizations, we assign $t = 0$ to the frame just prior to discharge, a convention followed throughout the paper. It is to note that, here, we do not consider the effect of the initial contact angle (or equilibrium contact angle, $\theta_{\text{eq}}$) of the droplet while describing the hydrodynamics observed. We put forward a discussion on the same in Sec. SV within the Supplemental Material [53].

Further, in Sec. SVI within the Supplemental Material [53], we show an order of magnitude analysis of the different forces for a sessile droplet deforming under the influence of the electric field. The study reveals that, during the electric discharge, the magnitude of the gravitational force is significantly smaller than the capillary and electric field forces under the proposed experimental conditions [63]. Thus, the dimensionless numbers associated with the gravitational force have not been considered in the present study. In what follows, we show the salient features of the postdischarge electrohydrodynamic (EHD) behaviors with the variations in the electric field intensity alongside the viscosity, surface tension, and the electrical conductivity of the droplet.

### A. Initial dynamics of discharge and generation of cavitation bubbles

#### *1. Dielectric barrier discharge*

The electric field discharge due to the local breakdown of the dielectric film, beyond a critical intensity ($\Psi \geq \Psi_{\text{cric}}$), helps in confining a significant amount of energy inside the droplet fluid. Such discharges are supplemented by the production of "plasma channels" in the droplet with the occurrence of visible flashes, as shown in Fig. 2(a). In a way, the intensity of flash can be treated as an indicator of the strength of discharge. However, the location of discharge is not only difficult to trace, but also the sequence of events after the discharge does not show up the same degree of repeatability even when the experimental conditions remain similar. Interestingly, a series of experiments and simulations uncover that the initial positioning of the anode is one of the crucial factors in fixing the location of discharge. Postdischarge, the plasma channels manifest within a very short time span ($t_{\text{disc}}$) before expanding either to a critical size to form a local nucleus or bridge the gap between the electrodes. Notably, the discharge and plasma formation have a time scale much lower than the same of the hydrodynamics of droplet actuation. Thus, during the experiments, multiple discharge cycles are also a possibility within the droplet in contrary to the events of spark discharges [28,64]. An evaluation of the specific input energy for discharge, $E_d/m$, can be compared with the specific energy of the ejected mass ($E_k/m$) to calculate the mechanical energy conversion efficiency of the reported hydrodynamic phenomena.

#### *2. Dynamics of bubble formation*

Previous studies indicate that such dielectric breakdown by electric field discharge favors the formation of single or multiple cavitation bubbles inside the droplet [28,65]. However, the origin of the cavitation bubbles in the discharge cycles host a complex physics, as argued by several existing literatures [65,66]. In particular, we find the "thermal" model to be relevant to the present experimental observations [28,66], which suggests that the bubbles are generated by the localized heating of the liquid volumes through the rapid flow of electrical current near the discharge hotspots. The intensely localized electric field of large power density at the tip of the sharp anode, as well as

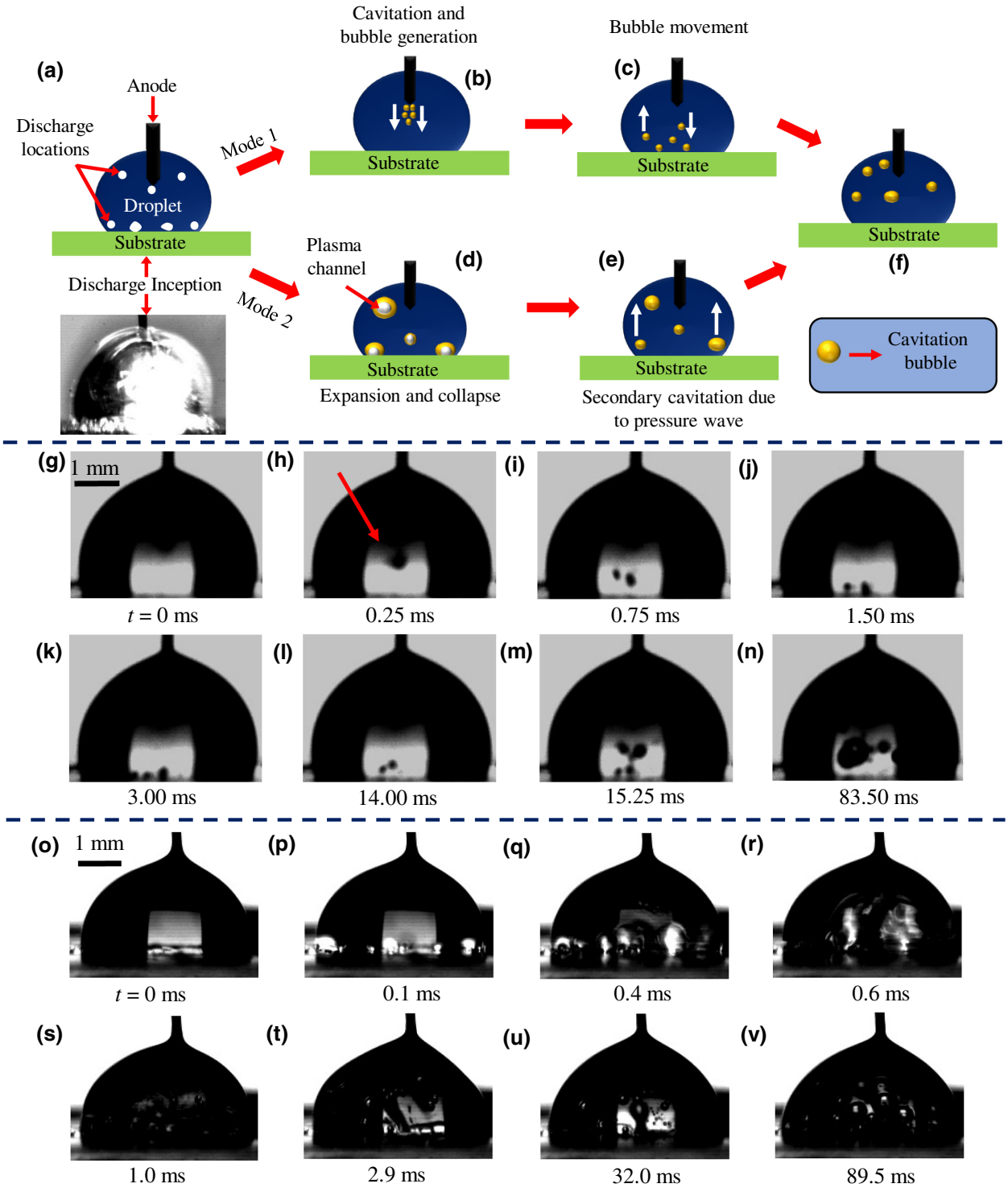


FIG. 2. (a)–(f) Schematics of the "mode 1" and "mode 2" of bubble formation after discharge in the droplet. (a) Also showing the experimental footage of the discharge covering the droplet. (g)–(n) Experimental snapshots of bubble formation inside a DI-water droplet (solution 4, Table II) in "mode 1." The red arrow on the image (h) marks the onset of bubble formation. (o)–(v) The bubble formation inside a droplet of glycerol (65%) and water (35%) mixture (solution 7, Table II) in "mode 2."

the microscale asperities in the cathode, generate discharge channels, which in turn facilitates local heating of liquid to nucleate a number of bubbles of high thermal energy [66] and subsequently the multiple hotspots. Consequently, the thermally simulated bubbles trigger observed hydrodynamic phenomena. This is in stark contrast to the situations

that arise with the use of pulsed laser [8,34] or thermal excitation [67] or electric spark [28,64], which facilitate the formation of a single isolated bubble within a sessile or suspended droplet.

Notably, the experiments conducted for the present study show two distinct modes of discharges and subsequent cavitation bubble formations, (i) from the tip of the "anode" or (ii) from the physical or chemical heterogeneities of the "cathode," as depicted schematically in Figs. 2(a)–2(f). In "mode 1," the bubbles are ejected as a cluster from the sharp tip of the anode and pushed towards the cathode at a velocity of approximately 1 m/s. After hitting the cathode, the cavitation bubbles randomly bounce back to the liquid-gas interface, often after coalescing, to cause the reported hydrodynamic phenomena. The path in the schematic images, $a \rightarrow b \rightarrow c \rightarrow f$, depicts this mechanism wherein the arrows mark the direction of the movement of bubbles and their coalescence within the droplet. The corresponding experimental visuals are shown in Figs. 2(g)–2(n) (see also Movie 1 within the Supplemental Material [53]), where the electric discharge is generated within a 5-$\mu$l conducting droplet (solution 4, Table II) at an electric field intensity, $\Psi = 13.2$ kV/cm. The red arrow on Fig. 2(h) indicates the onset of bubble ejection. In this mode, the discharge cycle is completed within, $t_{\text{disc}} = 13$ ms [up to Fig. 2(m)]. Figure 2(n) shows a collection of coalesced bubbles within the droplet after multiple discharge cycles in the case of droplets with high electrical conductivity.

On the other hand, "mode 2" is schematically depicted by the path $a \rightarrow d \rightarrow e \rightarrow f$ , in Fig. 2, wherein the bubbles are preferably generated near the cathode before they undergo expansion and collapse. The experimental snapshots in Figs. 2(o)–2(v) (see also Movie 2 within the Supplemental Material [53]) show such bubble formation after discharge in a 5-$\mu$l droplet of glycerol (65%) and water (35%) mixture (solution 7, Table II) when, $\Psi = 13.51$ kV/cm. The discharge hotspots can be identified by the bright flashes in Fig. 2(p). The expansion and collapse of the cavitation bubbles can be followed in Figs. 2(p)–2(s). Prior art suggests that the case shown in Fig. 2(s) can cause release of acoustic pressure waves (APW) or shock waves [28,67–69], which reflect back and forth inside the liquid volume to stimulate the phenomena exhibited. Previous studies also indicate that such confined movements of the pressure waves result in the "secondary cavitation," as seen in Fig. 2(t) [28,67]. In a way, "microbubbles" or "secondary cavitation bubbles" are generated via the multiple excitation of the preexisting nuclei, e.g. dissolved gas and/or impurities, in the liquid volume, as the APW redistribute their energy after reflecting at boundaries [35,70]. The multiple reflections of APWs further facilitates the formation of a large cluster of these secondary bubbles within one discharge cycle in the droplet [28,70]. This is marked by the comparatively darker interior of the droplet [comparing Figs. 2(o) and 2(v)] after three discharge cycles at $t = 89.5$ ms.

The lifetime of the secondary cavitation bubbles, ($t_{\text{osc}}^{\text{sec}}$), is higher than the lifetime of primary ones, ($t_{\text{osc}}^{\text{pri}}$). This can be found out by considering the Rayleigh collapse time [71], $t_{\text{coll}}^{\text{pri}}$, of the latter, defined as the time required for a bubble at maximum radius, $r_b^{\max}$, to shrink to its next minimum, $r_b^{\min}$ (= 0), in a liquid of density $\rho$ under the static pressure, $P_{\text{stat}}$. Thus, for a water vapor bubble the collapse time is as follows:

$$t_{\text{coll}}^{\text{pri}} = 0.915 r_b^{\max} \sqrt{\frac{\rho}{P_{\text{stat}} - P_v}}, \tag{1}$$

where $P_v$ is the non-negligible water vapor pressure opposing the outer static pressure, $P_{\text{stat}}$. Considering, $P_{\text{stat}} =$ 100 kPa under atmospheric condition and $P_v = 3.2$ kPa, water vapor pressure at 25°C, the time period for the collapse of a, $r_b^{\max} = 1$ mm, bubble is $t_{\text{coll}}^{\text{pri}} \sim 0.11$ ms, leading to $t_{\text{osc}}^{\text{pri}} (= 2t_{\text{coll}}^{\text{pri}}) \sim 0.22$ ms, a value closer to the experimentally observed values (approximately equal to 1.0 ms) in Figs. 2(p)–2(s). However, the difference in the magnitude of both experimentally and theoretically observed values of $t_{\text{osc}}^{\text{pri}}$ arise from not considering the effect of viscosity and multiple bubble interaction during the analysis of the concerned phenomena. In contrast, the secondary cavitation bubbles are seen to have a lifetime, $t_{\text{osc}}^{\text{sec}} \sim O[10^2$ ms], for the highly viscous case shown in Figs. 2(o)–2(v). It may be noted here that $r_b^{\max}$ of the microbubbles are in the range of 0.1 to 1 mm, whereas the primary cavitation bubbles can expand to a size equivalent to the droplet.

Further, for highly viscous droplets (solution 9, Table II), the primary cavitation bubble is not able to shrink to, $r_b^{\min} = 0$, after one oscillation cycle [see Figs. 3(a)–3(d) and Movie 3 within the Supplemental Material [53]]. This can be linked with the lower discharge energy and enhanced viscous dissipation within the droplet. However, the bubble radius reaches new maxima in the next few cycles, as can be seen in Fig. 3(g). Figure 3(g) clearly shows a damping behaviour as the bubbles oscillate in the viscous surrounding. We have been able to track the $r_b(t)$ only up to three discharge cycles beyond which the spatial resolution of the experimental images makes it difficult to track. Interestingly, similar behavior has been reported recently for cavitation bubbles in an elastic matrix [72].

The discussions above also highlight the limits of the present experimental setup to provide a comprehensive picture of the underlying physical processes associated with the discharge cycles and subsequent oscillatory behaviors of the cavitation bubbles [73]. This is because, the proposed experimental setup is equipped to capture the time scales for hydrodynamics features ($t_{\text{hydro}}$), which is much larger than the discharge or oscillatory ones,

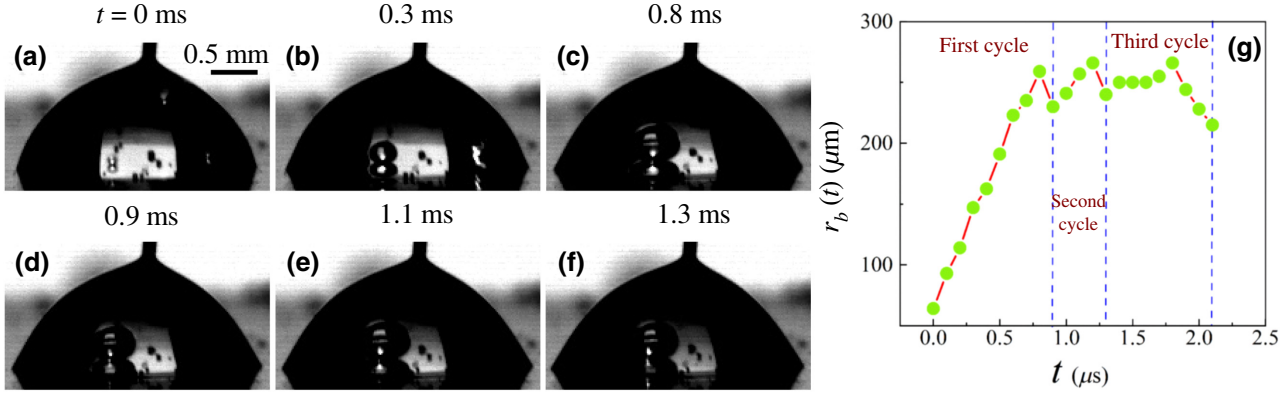


FIG. 3. (a)–(f) Growth dynamics of a cavitation bubble after discharge inside a highly viscous drop of glycerol (80%)-water (20%) mixture (solution 9, Table II) postdischarge. The droplet volume is 5 $\mu$l, whereas the electric potential applied is $\psi = 500$ V ($\Psi = 16.98$ kV/cm). (g) The temporal variation of the radius of the cavitation bubble ($r_b$) oscillating inside a highly viscous liquid.

$t_{\rm disc} < t_{\rm osc}^{\rm pri} \ll t_{\rm hydro}$. Thus, we are able to elucidate several characteristic features of discharge-mediated jetting or crowning or bursting dynamics, as discussed in the following sections.

### B. Overview of the fragmentation regimes

The EHD features reported here, namely, jetting, crowning, and bursting, have been engendered by electrical discharge in the liquid droplet. In the "jetting" regime, a series of smaller volumes of the liquid masses are ejected from the main droplet matrix. On the other hand, "bursting" of the sessile droplet is an intense and fast phenomenon, which completely disrupts the cohesive forces of the droplet to eject the entire mass in the form of fine sprays of liquid droplets in a split second. The "crowning" can be considered as an intermittent regime with the formation of metastable liquid sheets from the drop-matrix during ejection, followed by the ejection of droplet masses before the collapse. During the multiple discharge cycles, there exists a possibility of witnessing a combination of the EHD features, when the other experimental conditions are kept similar. The experiments reveal that the droplet volume, viscosity, electrical conductivity, and field intensity are some crucial factors to fine tune the thermodynamics and kinetics of such jetting, crowning, bursting, and mixed regimes. For example, one can manifest all the regimes simply by tuning the intensity of the applied electric field, while keeping other parameters the same (detailed discussion in Sec. III G 1). Further, we are also able to tune the kinetics of such phenomena by changing the viscosity of the droplet. In what follows, we show that even the location of the anode (expressed in terms of the vertical distance between the electrodes, $h_e^* = h_e/r_d$) plays a crucial role in deciding the type of EHD pattern emerges.

For this purpose, in order to anticipate the postdischarge EHD scenario, we show some simulated results in Figs. 4 and 5, on the distribution of electric field at the instant of application, before discharge. The details of the geometry, meshing, governing equations, boundary conditions, and solution procedure of the simulations are provided in Sec. SVII within the Supplemental Material [53]. In particular, the simulations uncover the distribution of the equipotential lines and field vectors at different locations of electrode-droplet geometry. It is worth noting here that the conducting nature of the droplet favors the formation of a capacitor like configuration with the dielectric layer sandwiched between the electrode pairs to concentrate the EHD stress mostly across the former. The contours with vectors to the left of Figs. 4(a)–4(d) show such electric field distribution in the entire droplet-electrode setup, while the magnified pair of contours to the right shows the same in the dielectric layer under the anode (top image) and near the three-phase contact line (TPCL, bottom image). Figure 4(a) shows that when the anode tip is very close to the cathode, the field intensity is highest at the dielectric layer just under the tip. On the other hand, Figs. 4(b) and 4(c) show that, with the increase in the gap between the electrodes, not only the effective intensity of the electric field within the dielectric layer decreases but also the zone of maximum field intensity shifts towards the TPCL. Fig. 4(d) also shows that if the electrode is placed outside the droplet, the field intensity at the thin dielectric layer decreases drastically both under the anode as well as at the TPCL.

The results shown in Fig. 4 are further extracted for a better analysis in Fig. 5, wherein Fig. 5(a) schematically shows the locations *A*–*I* at the dielectric layer at which the data are extracted. Figure 5(b) shows the variation in the field intensity at some of these different locations ($x$) at different electrode distances, $h_e$ (or $h_e^*$). The figure suggests that for $h_e^* = 0.05$, the field intensity ($\Psi$) is highest under the anode (location *E*), whereas, beyond $h_e^* = 1.0$, the field intensity becomes highest at the TPCL. The plots

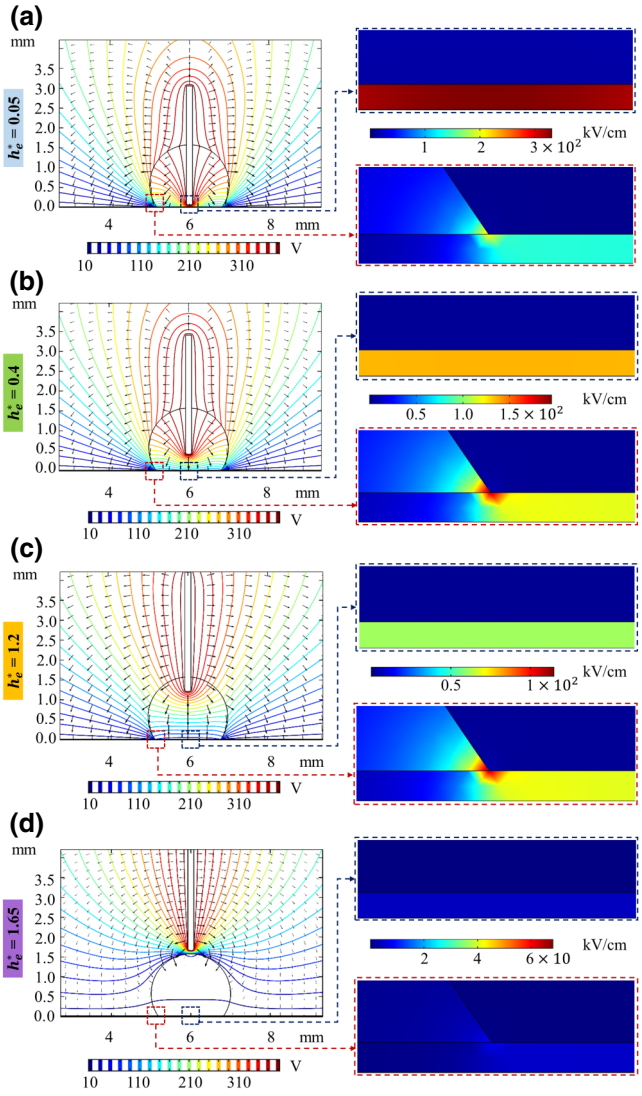


FIG. 4. Distribution of the electric field vector and equipotential lines when a potential, $\psi = 400$ V is applied to a droplet of radius, $r_d = 1$ mm, for different position of the electrode, $h_e^* =$ (a) 0.05, (b) 0.4, (c) 1.2, and (d) 1.65. The right-hand side of each image represents the enlarged view of the two boxed areas (in each plot), which shows the electric field distribution (surface plot) within the dielectric layer. The nondimensional electrode distance is $h_e^* = h_e/r_d$.

in Fig. 5(b) apparently speaks about the presence of two distinct regimes. For $h_e^* < 0.3$, the electric field is concentrated at the center of the droplet footprint (location $E$), which favors the formation of a strong discharge channel between the electrodes, originating from a single discharge hotspot. Such a discharge may favor the bursting of the droplet, as depicted in Fig. 5(d). Further, Fig. 5(d) shows that for $h_e^* > 0.4$, the electric field distribution may favor the formation of multiple discharge hotspots in the wetted area of the droplet, which may lead to the jetting regime. In the intermediate zone, $0.3 < h_e^* < 0.4$, one can observe both crown and jet formation, as depicted in Fig. 5(d). In essence, the results from the simulation and experiments, show a strong correlation between the predischarge electric field distribution and the observed EHD regimes, as summarized in Fig. 5(d). Furthermore, the size of the droplets also affects the effective electric field at different positions of the electrode. We show electric field strength at two locations of the dielectric layer, $\Psi_C$ and $\Psi_E$, for different droplet sizes in Fig. 5(c). The plots clearly show that as the droplet size decreases, the strength of the electric field increases at all the locations, thereby facilitating the bursting or liquid crown-formation events.

### C. Jetting regime

The discharge-mediated spatiotemporal evolution of a liquid jet originating from the free surface of a droplet (solution 5, Table II) is presented in Fig. 6 (see also Movie 4 within the Supplemental Material [53]). The results suggest that the mechanism of formation of such liquid jets are markedly different from the ones observed due to collapse of surface waves in atomization experiments [74]. However, the dynamics of the jet breakup are much akin to that of the reported work. Figure 6(b) shows that postdischarge, bubbles are generated at the hotspots (small white regions) immediately under the air-water interface of the droplet. The expansion and subsequent collapse of the bubble(s) stimulate the upward motion of the liquid jet [28,69,75]. Interestingly, we find the issuance of three jets in Fig. 6(c) marked by numbers 1–3, out of which two are growing along the cathode surface, while the other being released vertically along the anode, marked as 1. The experimental conditions ensure that multiple discharge locations are generated within the droplet, which in turn generates multiple bubbles with a lifetime of $t_{\rm osc}^{\rm pri} < 100$ $\mu$s, as indicated by the frames of Fig. 6. While the rapid expansion of these hot bubbles helps in creating the jets in all the directions, the anode helps one of the jets (1) to climb against gravity, as shown in Figs. 6(c)–6(j). The maximum upward velocity of the jet is found out as $U_j \sim 2.5$ m/s (suffix $j$ refers to jetting phenomena). The jet simultaneously develops a bulbous tip [refer Fig. 6(f)] while climbing up the electrode. The size of the tip increases until the jet reaches the maximum height [Fig. 6(j)] before it separates from the body of the primary jet as a result of "end-pinching" (marked by arrows) to form an isolated bulbous secondary droplet. After the bulbous secondary droplet is pinched off, the remainder of the jet traces back towards the liquid surface under the action of the capillary force. Subsequently, we also notice another pinchoff near the jet base in Fig. 6(k), giving birth to an additional secondary droplet [Fig. 6(l)].

However, it is not appropriate to assume that these discharge-mediated jets always ascend along the anode while moving upward. Even though the positioning of the anode is critical, the emergence of the jet is dependent

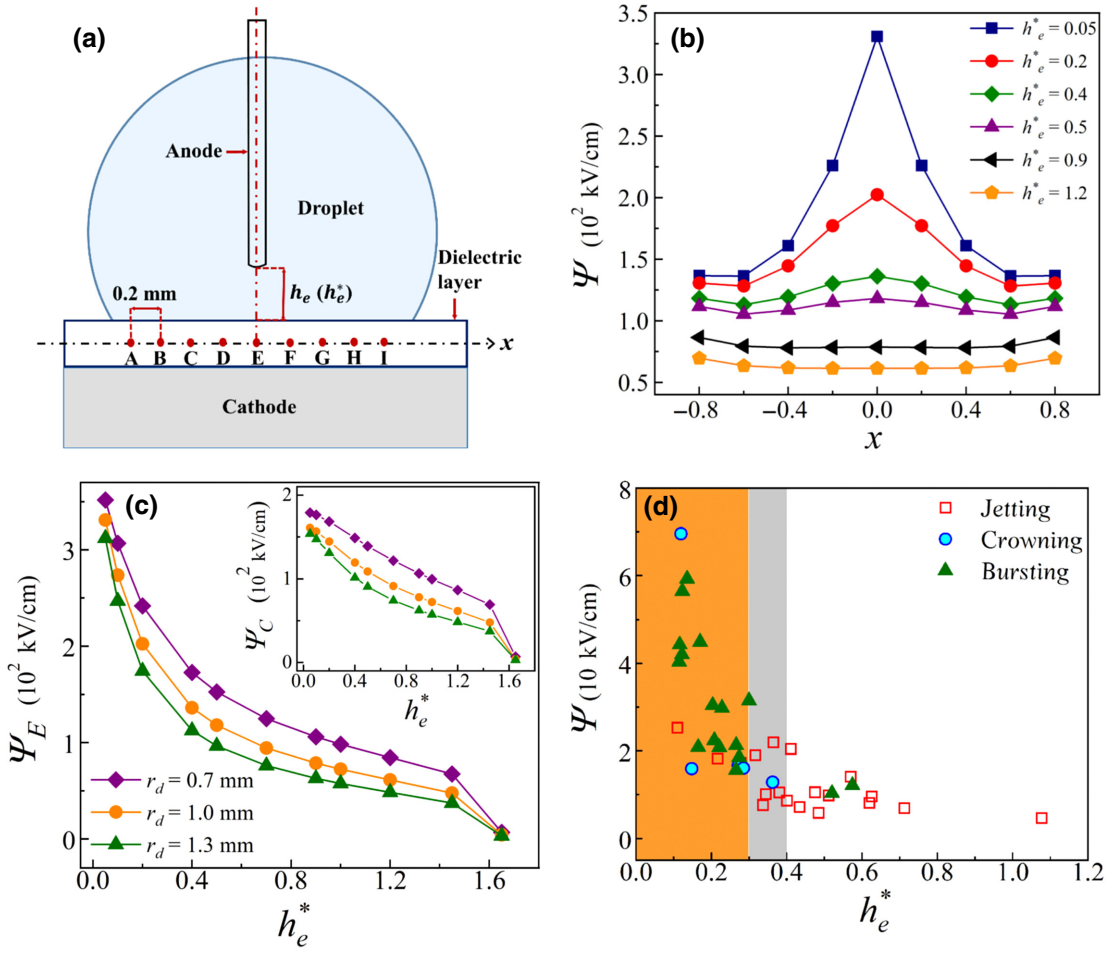


FIG. 5. (a) Schematic diagram showing the locations (*A–I*) in the dielectric layer, which are considered for the other plots. (b) The resulting field intensity ($\Psi$) inside the dielectric layer at the locations indicated in image (a) when, $\psi = 400$ V and the location of the electrode ($h_e^*$) is varied. (c) The variation of field intensity at location *E*, $\Psi_E$, (and *C* in the inset, $\Psi_C$) with $h_e^*$ for liquid droplets of different radius ($r_d$), while the electrode diameter is kept same (0.150 mm). (d) Experimental points showing different regimes, namely, jetting, crowning, and bursting, at different applied electric field, $\Psi$, with the variation in $h_e^*$.

on the location of the discharge and subsequent cavitation bubble dynamics. In Fig. 7 (and Movie 5 within the Supplemental Material [53]), we present a situation wherein the jet is not following the anode. Here discharge is generated within the droplet (solution 4, Table II) with the help of an electric field, $\Psi = 13.51$ kV/cm. Again, postdischarge, we notice the formation of multiple jets numbered as 1–3 in Fig. 7(d). The distinguishable primary jet, numbered as 1, has similar characteristics to that of the same shown in Fig. 6, with "capillary pinchoff" [refer to Figs. 7(e) and 7(g)] being the predominant mechanism droplet generation from an upward-moving jet. However, in later instances, after the generation of a couple of secondary droplets, the retracting jet is further disintegrated into multiple droplets, as shown in Figs. 7(i)–7(l). The jet breakup locations are marked with arrows. The maximum jet velocity for this case is found to be $U_j \sim 1.5$ m/s.

The breakup of the liquid thread during the jet formation follows the "end-pinching" mechanism identified by Stone *et al.* [76] and Vukasinovic *et al.* [74]. The similarity in the order of magnitude of the Ca($\eta U_j/\gamma \approx O[10^{-3}] \times O[10^0]/O[10^{-1}] \sim O[10^{-2}]$) also allows us to make an analogy with this already proposed mechanism. Briefly, the impulse from the cavitation bubbles collapsing inside the droplet pushes the liquid-air interface with a high momentum to form the jet. The fluid near the liquid-air interface ascends faster as compared to the fluid near the jet base or contact line owing to the less frictional resistance. Subsequently, the growing bulbous front moves away from the remainder of the jet at a much faster rate causing a gradual reduction in the neck radius and eventual pinchoff to form the secondary droplet. In this scenario, the necking of the jet grows further since the higher capillary pressure in the regions of smaller radius forces the fluid

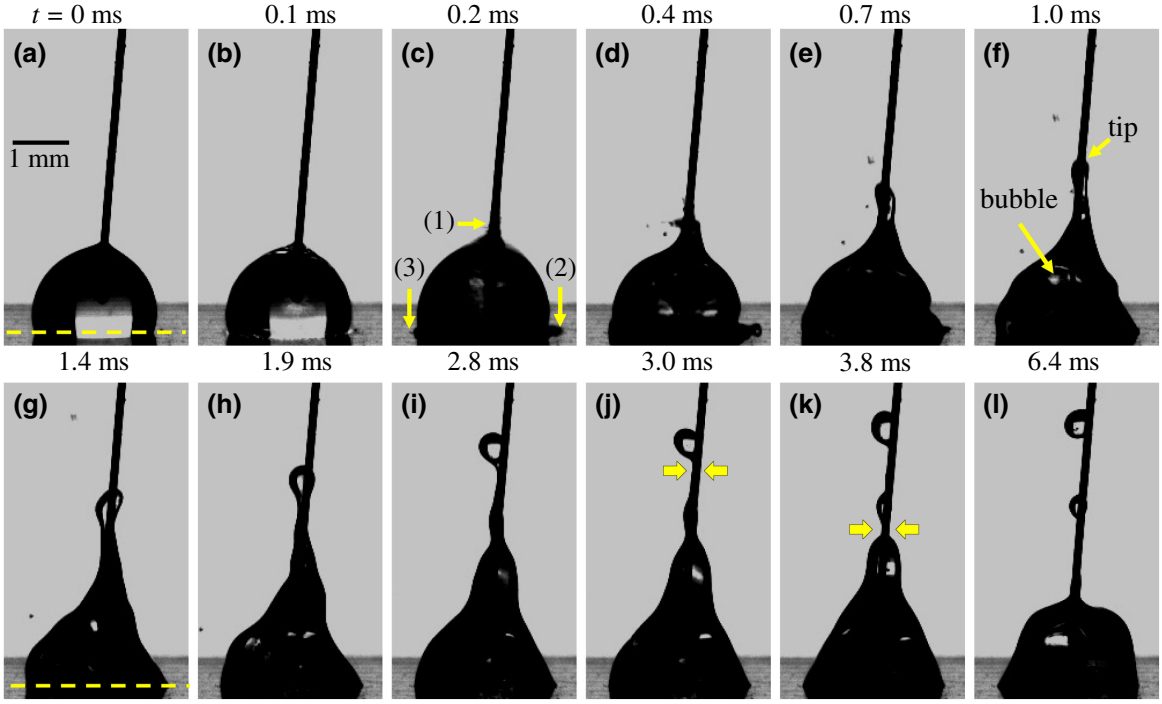


FIG. 6. Sequence of jet formation due to the electric discharge inside a droplet (solution 5, Table II) and subsequent breakup of the jet ejecting secondary droplets. Images (a)–(j) show growth of jet in which image (j) shows the pinchoff region, the area marked between the arrows indicating neck formation phenomena. Images (k),(l) show the second pinchoff event along with the separated secondary droplets. The other experimental conditions are $\psi = 1000$ V, $\Psi = 20.86$ kV/cm, $V_{\text{drop}} = 5$ $\mu$l, $C_s = 1.0$ M, and $\eta = 0.886$ mPa s. The yellow broken line shown in image (a) is considered as datum during jet height and velocity measurement.

to move towards the bulbous tip with a lower capillary pressure, as explained previously by Stone *et al.* [76]. The time scale for the postdischarge jet breakup approximately 1.5–3 ms matches with the theoretical capillary time scale, $t_{\text{cap}} \sim \sqrt{\rho r_j^3/\gamma} \sim O[10^{-3}$ s], where $r_j$ is the radius of the jet [77]. Considering the jets to be near-cylindrical one, the mass of the jets prior to secondary droplet generation can be evaluated as $m_j = 1.4 \times 10^{-7}$ kg, and $1.2 \times 10^{-7}$ kg, corresponding to Figs. 6 and 7, respectively. Accordingly, the maximum (average) kinetic energy of the jets is found to be $E_k^j = m_j U_j^2/2 \sim 4.7 \times 10^{-4}$ mJ ($3.13 \times 10^3$ mJ/kg) and $9.0 \times 10^{-5}$ mJ ($7.5 \times 10^2$ mJ/kg), respectively, depicting an (average) energy conversion efficiency of approximately 0.35–0.6% for the electric-discharge-mediated jet formation.

The size of the secondary droplets is found to be in the range of 0.2–0.5 mm. One significant observation for the jet breakup is the deviation from the "Plateau-Rayleigh instability" through the magnification of the capillary waves [78]. In a way, the elongated liquid jet generated after discharge breaks via the end-pinching mechanism to form the secondary droplets while the remaining part of it recoils back towards the primary droplet. It is well known that for the capillary instability to grow, the wavelength ($\lambda$) of disturbance has to be more than the circumference ($2\pi r_j$) of the jet, i.e., $\lambda/r_j \geq 9$ [79,80]. The liquid jets shown in Figs. 6 and 7 have aspect ratio $A_R = L/d_j = O(6) - O(9)$, where $L$ is the maximum length of the liquid jet. Thus, the length scale is found to be much smaller than the length required for the growth of the conventional Plateau-Rayleigh modes. Apart from the formation of the regular jets, an array of microjets also appears along the liquid-air interface after the discharge, which has a significant contribution towards the effective atomization or mass loss. We put forward a dedicated section (Sec. III F) later to discuss the dynamics of microjets during electric-discharge-mediated atomization.

### *1. Dynamics of viscous jets*

Figure 8 shows that the dynamics of the jets can be significantly affected by the viscosity of the droplet. The high-viscosity droplet electrowets in the predischarge phase before forming the jet after the discharge. Figures 8(a)–8(f) (see also Movie 6 within the Supplemental Material [53]), and Figs. 8(g)–8(l) (see also Movie 7 within the Supplemental Material [53]), show the evolution of liquid jets of two different viscosities (solution 6 and solution 9, Table II). The cylindrical jets, for Oh = 0.022 and 0.21, move upward for a considerably longer time as compared to the previously shown less viscous jets in Figs. 6

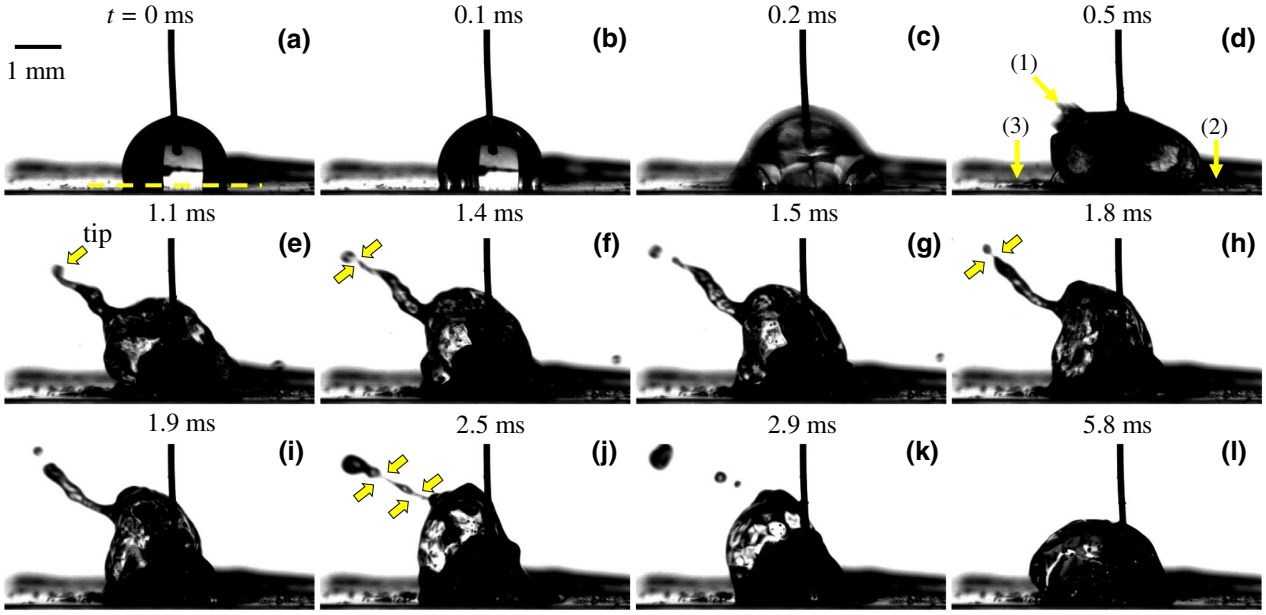


FIG. 7. (a)–(l) Sequence of liquid-jet formation due to the electric discharge inside a droplet (solution 4, Table II) and subsequent breakup of the jet ejecting secondary droplets after discharge. The first pinchoff event is marked by the arrows in image (e), while the pair(s) of arrows in images (g),(i) mark(s) different breakup events of the liquid jet. The other experimental conditions are $\psi = 800$ V, $\Psi = 13.51$ kV/cm, $V_{\text{drop}} = 5$ $\mu$l, $C_s = 0.5$ M, and $\eta = 0.887$ mPa s. The yellow broken line on the image (a) represents the datum.

and 7. However, for Oh = 0.022, the liquid jet continuously develops a bulbous tip until about 12 ms, as shown in Fig. 8(d). The stages are composed of jet ascending, bulbous tip formation, jet breakup at the base, end pinching, capillary thinning, and Plateau-Rayleigh instability, as schematically described in Fig. 8(m). The arrows shown in Fig. 8(d) indicate the first breakup of the liquid jet at its base. Figure 8(e) shows the separation of bulbous tip from the jet through "pinchoff" before moving upward, while the separated jet in the middle [neck to tail, Fig. 8(m)] retracts downward. It develops a dumbbell-shaped intermediate structure in order to relax the high surface curvatures generated near the breakup points. Finally, the intermediate dumbbell-shaped flow morphology undergoes disintegration to form two more secondary droplets due to the Plateau-Rayleigh instability. The size of the secondary droplets is in the range of 0.4–0.6 mm, which helped in estimating the mass of the liquid jet to be approximately $1.34 \times 10^{-6}$ kg. The maximum kinetic energy of the jet is found to be approximately $2.5 \times 10^{-3}$ mJ ($1.90 \times 10^{3}$ mJ/kg), yielding an energy conversion efficiency of approximately 1.44% for an input energy, $E_d \approx 1.32 \times 10^{5}$ mJ/kg.

Again, increase in the viscosity by an order (Oh = 0.21), results in the formation of a longer but slender jet, as seen in Figs. 8(g)–8(l). The jet thins while moving upward, and subsequently, disintegrate into parts, as shown in Fig. 8(i). The absence of the bulbous tip in a highly viscous jet is a substantial difference from the previous experimental realisations. In this case the highly viscous jet attains a maximum velocity of approximately 4.7 m/s. The arrows in Fig. 8(j) mark the point of detachment of the jet from its base. The secondary drop formation due to Plateau-Rayleigh instability becomes more prominent after this point, as shown in Figs. 8(k) and 8(l). The typical size of the secondary droplets is found to be approximately 0.2–0.35 mm.

Notably, Vukasinovic *et al.* [74] have previously shown that the first breakup point for an upward moving viscous jet appears at the base of the jet before undergoing various instabilities to form secondary droplets. The same phenomenon is observed in Figs. 8(a)–8(f). The Plateau-Rayleigh instability is found to dominate once the thread is detached from the base. However, a further increase in the viscosity by an order (Oh = 0.022 to 0.21) accelerates the thinning of the emerging cylindrical jet from the base, which in turn favors the growth of the capillary instabilities from the very beginning owing to the very high aspect ratio of the latter ($A_R \sim 100$). As a result, the first breakup of the jet takes place simultaneously with its detachment from the base, before multiple equally spaced secondary droplets are generated within a few milliseconds. Figure 8(n) traces the trajectories of three characteristic points during the shape evolution of the viscous liquid jets, namely, the tip, tail, and neck, as indicated in the schematic, Fig. 8(m). In this plot, the point, $t = 0$, marks the instant prior to discharge while the surface of the isolator is considered as $h_j = 0$, to make the distance absolute. The three different colors depict three cases with different viscosity values, whereas the different symbols, namely square box

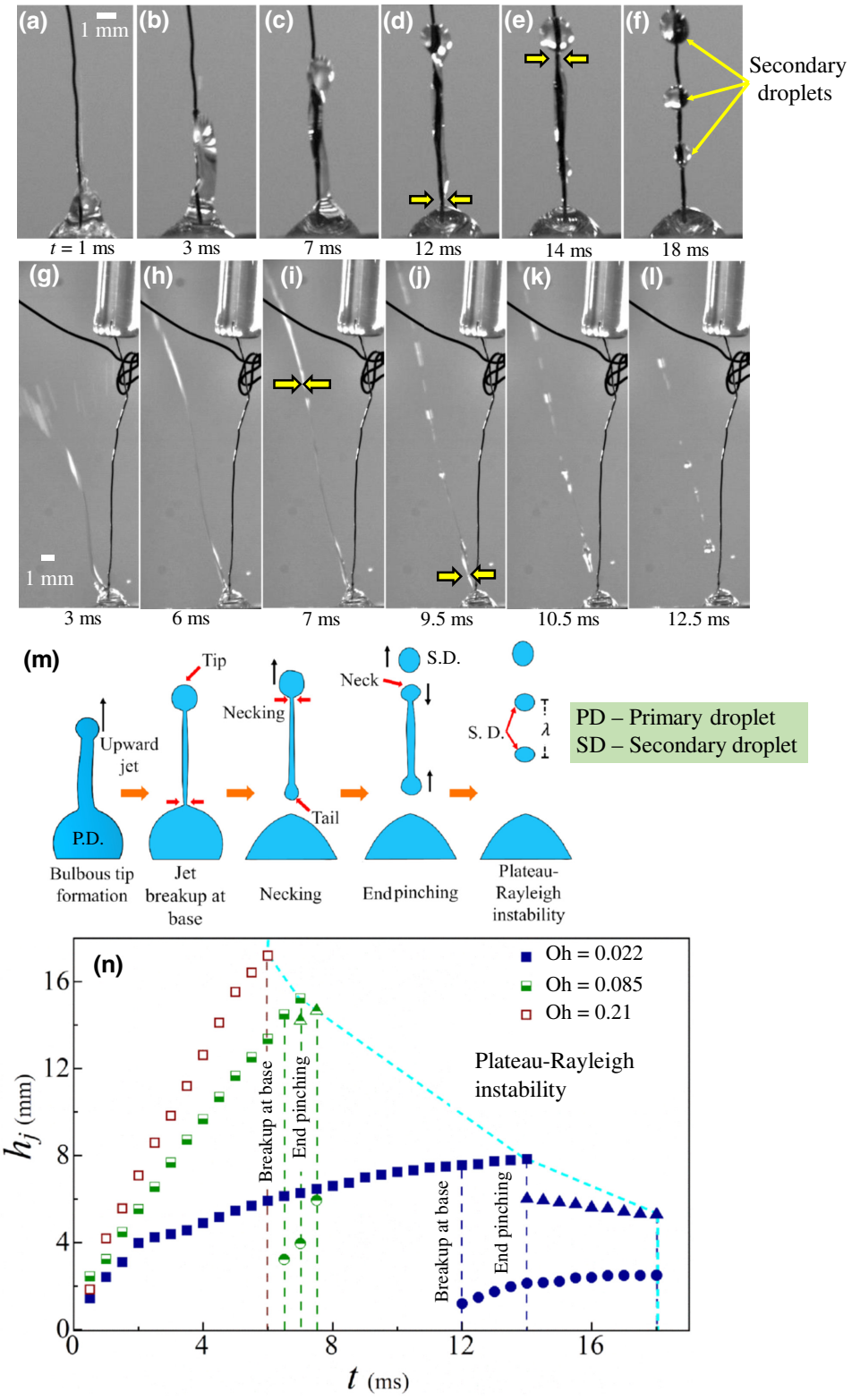


FIG. 8. Images (a)–(f) show the time evolution of a jet originating from a droplet with moderate viscosity subjected to an electric discharge. Experimental conditions are $\psi = 500$ V ($\Psi = 7.06$ kV/cm), $V_{\text{drop}} = 5$ $\mu$l, $C_s = 0.1$ M, and $\eta = 6.88$ mPa s. Images (g)–(l) show the time evolution of the jet formed, when a very high-viscosity droplet is subjected to an electric discharge. The experimental conditions are $\psi = 500$ V ($\Psi = 9.19$ kV/cm), $V_{\text{drop}} = 5$ $\mu$l $C_s = 0.1$ M, and $\eta = 66.96$ mPa s. The arrows mark the position of jet breakup at different instants. Image (m) schematically describes the underlying mechanism of breakup of a viscous jet and subsequent formation of secondary droplets from the jet. Image (n) shows characteristic trajectories of three different positions of a viscous thread, namely, the tip of thread (■), the tail of unbroken thread (●), and neck (▲) for droplets of different viscosity (represented by different colors as well as symbols). The broken lines differentiate the time of occurrence of events.

(■), circle (●), and triangle (▲), refer to the tip of the thread, the tail of the unbroken thread, and neck positions, respectively. The vertical broken lines demarcate the aforementioned events observed during the shape evolution of the viscous jets after discharge.

Figure 8(n) exhibits a few exciting observations for the discharge-mediated jet formation. Firstly, the initial slope ($t < 2$ ms) of the trajectories indicate an early acceleration of the jets. This also hints about the inertia-dominated jet dynamics, immediately after the discharge. For the

high-viscosity solutions (Oh $\geq$ 0.1), the acceleration continues until the first breakup point, and Plateau-Rayleigh instability takes place immediately after its detachment from the base. Also, the rapid thinning of the jet facilitates the growth of unstable wavelengths to generate a greater number of secondary droplets. However, for moderate viscosity of the droplet (Oh = 0.022), the slope of the jet trajectory decreases after the initial inertia-dominated phase ($t < 2$ ms), indicating a slower jet dynamics and thinning. Comparing the dynamics of jets for the less viscous (see Figs. 6 and 7) and more viscous (see Fig. 8), it can be inferred that the electric discharge can generate thinner and longer liquid jets in the latter situation. Also, as observed, the propensity of the generation of both high-aspect-ratio jets, $A_R \geq O(15)$, and secondary droplets increases with the increase in viscosity of the droplet. We demarcate the region of Plateau-Rayleigh instability (RP instability) for jets of different viscosity by the broken line in Fig. 8(n). Here, we show the results from single experimental realization to give a qualitative overview of the viscous jet dynamics.

The experiments further confirm that the increase in viscosity of the experimental solution kinetically stabilizes the liquid jet, which in turn facilitates its elongation in the vertical direction. Consequently, the elongated jets favor the growth of capillary waves to form multiple secondary droplets after the first one is formed following the "end-pinching" mechanism. For the systems under consideration, a pair of jetting regimes can be elucidated from the magnitude of the Ca, to differentiate the underlying mechanism of secondary droplet formation. For example, when Ca $\ll$ 1, for the experiments shown in Figs. 6 and 7, fast-moving jets can generate bulbous secondary droplets through capillary pinchoff, indicating the dominance of inertia over the surface-tension force. In comparison, increase in the viscosity of the droplet prompts the appearance of the other regime corresponding to Ca $\geq$ 1, where the jets initially detach from the base before the dominance of the capillary force over the inertia helps in breaking them into multiple secondary droplets via Plateau-Rayleigh instability.

We also analyze the temporal variations in the jet height, $h_j$, until the instant of the first breakup for solutions having different viscosity, as shown in Fig. 9(a). Here, $\tau$ is the nondimensional time scale derived as $\tau = t/t_{\rm vis} = t/(\eta L/\gamma)$, with $t_{\rm vis}$ being the visco-capillary time scale [81] and $h_j^* = h_j/r_d$ is the nondimensional jet height. The figure confirms that, with an increase in the solution viscosity, the resulting liquid jets become faster accompanied by continuous thinning. Interestingly, all the nondimensional plots collapse into a single curve as shown in the inset of Fig. 9(a) following the unified power law, $h_j^* \propto a\tau^b {\rm Oh}^c$. The regression analysis of the experimental data gives the coefficients as $a = 20.169 \pm 1.582$, $b = 0.436 \pm 0.047$, and $c = 0.781 \pm 0.060$. Notably, the strong

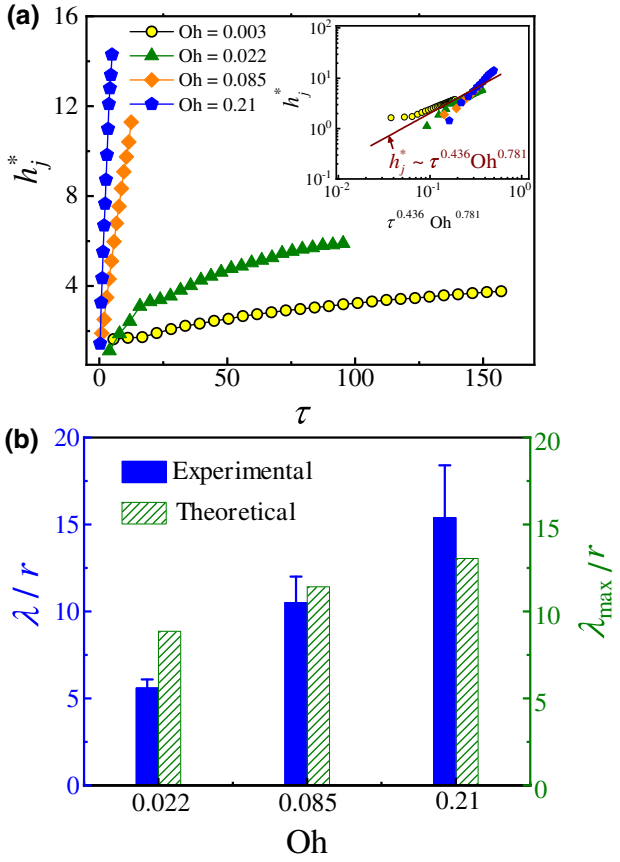


FIG. 9. Plot (a) shows the variation in the nondimensional jet height ($h_j^*$) before the first breakup with time ($\tau = t/t_{\rm vis}$) when electric discharge is instigated inside the droplets of different viscosity (solutions 5, 6, 8, and 9, Table II). Here, $t_{\rm vis} = \eta L/\gamma$ is the viscous time scale corresponding to the experimental conditions. The plot in the inset shows the merging trend of the experimental data points following a unified scaling law, $h_j^* = a\tau^b {\rm Oh}^c$, with coefficients: $a = 20.169 \pm 1.582$, $b = 0.436 \pm 0.047$, and $c = 0.781 \pm 0.060$. Plot (b) shows the variation in the normalized spacing of the secondary droplets—experimental ($\lambda/r$) and theoretical ($\lambda_{\rm max}/r$) with Oh, where $\lambda$ and $r$ are the average spacing and radius of secondary droplets, obtained from experiments, while $\lambda_{\rm max}$ is obtained from the theoretical analysis. Here, $\lambda_{\rm max}$ signifies the wavelength of the fastest-growing disturbance responsible for the breakup of the thread. The Oh number is calculated based on the initial equilibrium radius of the primary droplet ($r_d$). The experimental conditions are $\psi = 500$ V (all three cases, except for solution 5, where $\psi = 1000$ V), $V_{\rm drop} = 5$ $\mu$l, and $C_s = 0.1$ M.

dependency of the jet height on the Oh is reflected from the magnitude of the coefficient $c$, which further explains the reason behind the elongated jets observed in high viscosity. Again, Fig. 9(b) shows the variation in the normalized spacing of the secondary droplets, $\lambda/r$, with Oh in which the experimental and theoretical values are plotted in blue and olive, respectively. The details of the theoretical treatment to calculate the most unstable wavelength

($\lambda_{max}$) are provided in Sec. SVIII within the Supplemental Material [53]). The plot suggests that $\lambda/r$ increases monotonously with an increase in viscosity of the primary droplet, which is in good agreement with the theoretical predictions from the Plateau-Rayleigh instability of viscous jets [82,83].

### D. Crown-formation regime

Figure 10 (see also Movie 8 within the Supplemental Material [53]) shows a sequence of images of liquid crown formation when a 5-$\mu$l droplet of 0.5 M KCl solution (solution 4, Table II) is exposed to a discharge of energy, $E_d \approx 5.28 \times 10^5$ mJ/kg. The figure suggests three stages of crown formation, (i) onset with a cohesive failure of the droplet after discharge, (ii) formation and expansion of liquid sheet to form a crown, and (iii) secondary droplet generation from the rim of the crown before complete sealing and collapse. In the first stage, the cavitation bubble formed due to the discharge is expected to undergo a rapid expansion to cause a cohesive failure of the droplet, as observed in Figs. 10(a) and 10(b). Here, we can intuitively argue that the rupturing of the liquid-vapor interface takes place at a later stage of bubble expansion, thus creating a lower pressure difference between the bubble interior and surrounding air at the time of rupture. This further favors the formation of a crown, analogous to the phenomenon reported by Avila & Ohl [34] in their work on laser-induced droplet fragmentation.

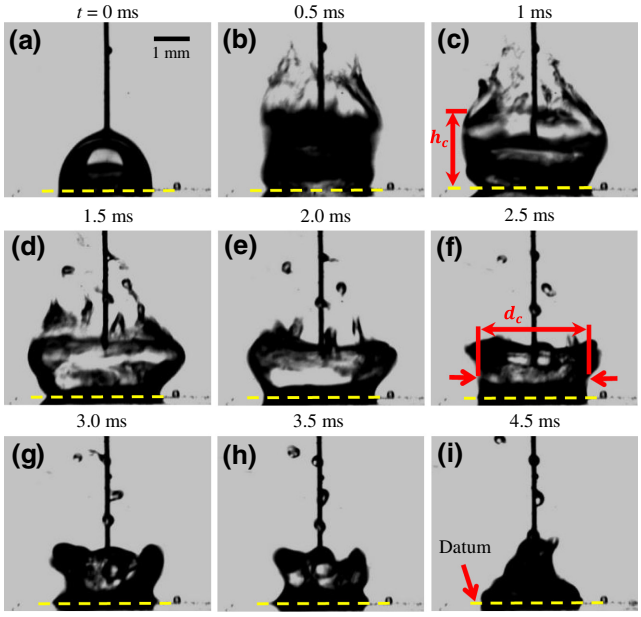


FIG. 10. Images (a)–(i) show the time evolution of the interface of a drop of KCl solution (solution 4, Table II), subjected to an electric field discharge, leading to the formation of a liquid crown. Experimental conditions are $\psi = 1000$ V, $\Psi = 9$ kV/cm, $V_{drop} = 5$ $\mu$l, $C_s = 0.5$ M, and $\eta = 0.887$ mPa s. Images (c),(f) show the positions of measurement of the crown height, $h_c$, with respect to a datum marked by the yellow broken line, and neck diameter (or radius), $d_c$ (or $r_c$), respectively.

In the second stage, the cylindrical liquid sheet stretches vertically as well as expands in a radially outward direction, as seen in Figs. 10(b)–10(d). The liquid sheet expands until 1.5 ms, which is continually opposed by the capillary forces. While stretching, the sheet progressively develops a liquid rim as well as thin ligaments due to continuous accumulation of fluid mass, as visible in Figs. 10(b) and 10(c), in a similar fashion to that of liquid splash events [84]. The liquid rim grows in size with time before experiencing capillary instability leading to the formation of an array of ligaments at the periphery, as seen in Fig. 10(d). The ligaments further generate secondary droplets via "capillary pinchoff," which are ejected away from the rim. The experiments uncover that the maximum velocity of the liquid sheet during the early expansion phase reaches $U_c^e \sim 0.8$ m/s.

In the third stage, the sheet starts collapsing or shrinking towards a common center under the effect of surface tension, as shown in Figs. 10(e)–10(i). One significant observation of this collapsing phase is the formation of a "necking regime," which continuously shrinks till the total collapse of the crown, marked by the red arrows in Fig. 10(f). Figures 10(c) and 10(f) indicate the way we define the height ($h_c$) and diameter ($d_c$) of crown (also referred to as "neck diameter") as it approaches sealing phase. The temporal variations in the neck radius further reflect the characteristics of the collapsing phase of the crown, which shall be discussed in the context of Fig. 12. The maximum shrinking velocity of the liquid sheet is approximately 1 m/s. Experiments uncover that the typical time scale for the expansion phase, $\approx 1.5$ ms $\approx 0.3$ $t_{sheet}$, is substantially less than the collapsing phase, $\approx 4$ ms $\approx 0.7$ $t_{sheet}$, indicating the dominance of capillary forces over the inertial force within the lifetime of the liquid sheet ($t_{sheet}$) forming the crown. The aforementioned features are also reported during crown formation by laser irradiation or thermal exposure [34,85].

The experimental time scale associated with the crown formation can be obtained from the balance of driving electric field force and restoring viscous and capillary forces. For example, the theoretical time scale, $t_{exp} = \left(\epsilon_0 \epsilon_p r_d \Psi^2/\gamma\right)\left(\eta L/\gamma\right) = \text{Bo}\, t_{vis} = 3.25$ ms, is found to be in close agreement with the experimentally observed time period of the inertia-driven expansion phase (1.5 ms) of the crown regime. Here $t_{vis}$ is the visco-capillary time scale related to the initial expansion of the crown. Similarly, the time scale for the collapse of the crown is obtained from the interplay between the driving inertial force to the restoring surface-tension force. The time scale for such a process is evaluated as [34] $t_{cap} = \sqrt{1/6}(\rho r_c^3/\gamma)^{1/2}$, where $t_{cap}$ corresponds to the time required for a fluidic

crown of neck radius, $r_c$ to retract itself towards a common center, thereby converting the surface energy to the inertial one. Substituting the necessary values, we obtain $t_{cap} = 2$ ms, which agrees closely with the experimental value (2.5 ms). In addition, the typical dimensions and physical properties of the droplet, $L = O[10^{-3}$ m], $U = O[10^{0}$ m/s], $\rho = O[10^{3}$ kg/m$^3$], $\gamma = O[10^{-1}$ N/m], $\psi = O[10^{3}$ V], and $\eta = O[10^{-3}$ Pa s] lead to Bo $= O[10^{3}]$, and Ca $= O[10^{-2}]$, which endorses the dominance of electric field and surface-tension forces over the inertial one in this breakup regime.

In the experiment shown in Fig. 10, the average height of the liquid sheet composing the crown wall, $h_c$ is approximately 2 mm, at the end of expansion stage [refer Fig. 10(d)]. Again, the velocity of retraction of the liquid sheet, $U_c^r$ is found to be approximately 0.9 m/s, which helps in obtaining the thickness of the sheet, $\delta \approx 0.2$ mm, from the force-balance expression proposed by Taylor [86], $U_c^r = \sqrt{2\gamma/\rho\delta}$. Therefore, the mass of the crown can be evaluated as $m_c \sim 2\pi\rho\delta h_c r_c \sim 4.95 \times 10^{-6}$ kg, where $r_c$ is the hollow radius of the crown [87]. The kinetic energy corresponding to the maximum expansion velocity of the crown ($U_c^e \sim 0.8$ m/s) is found to be $E_k^c \sim m_c(U_c^e)^2/2 \sim 2.08 \times 10^{-3}$ mJ ($4.16 \times 10^2$ mJ/kg), which is approximately 0.1% of the discharge energy, $E_d = 5.28 \times 10^5$ mJ/kg. Furthermore, the average diameter of the secondary droplets generated through this breakup mode is approximately 0.3 mm, which is approximately 10% of the initial drop diameter. The experiments suggest that the electric discharge within a liquid droplet is capable of disturbing the restoring influence due to the surface-tension force to develop a crown morphology with a higher surface-to-volume ratio and irregular shape. Even such an irregular crown can be made more regular by enhancing

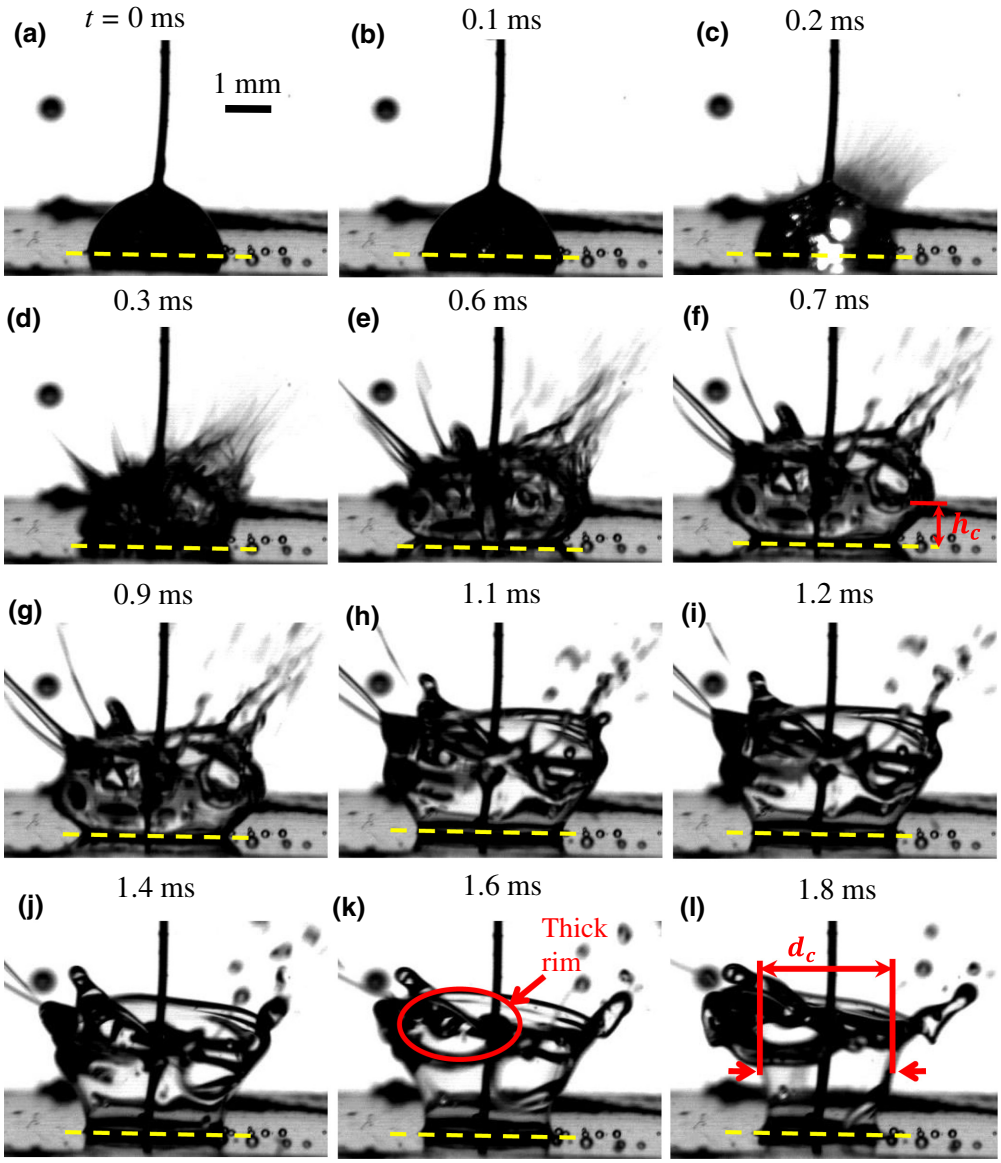


FIG. 11. Images (a)–(l) show the spatiotemporal evolution of a high-viscosity droplet of aqueous KCl solution and glycerol mixer (solution 7, Table II) subjected to an electric discharge. Experimental conditions are $\psi = 800$ V, $V_{drop} = 3$ $\mu$l, $C_s = 0.1$ M, and $\eta = 18.25$ mPa s. Image (a) shows the initial shape of the drop prior to discharge, images (b),(c) show propagation of discharge within the drop and initiation of crown formation, images (d)–(g) show the expansion of the crown, and images (h)–(l) show the sealing and collapse of the crown. Images (f),(l) show the positions of measurement of the crown height, $h_c$, with respect to a datum marked by yellow broken line, and neck diameter (or radius), $d_c$ (or $r_c$), respectively.

the droplet viscosity, as shown in Fig. 11 in the following Sec. III D 1.

#### *1. Crown dynamics at higher viscosity*

The shape evolution of a droplet with higher viscosity, for a discharge energy of $E_d \approx 4.82 \times 10^5$ mJ/kg (solution 7, Table II) is presented in Fig. 11 (see also Movie 9 within the Supplemental Material [53]). The enhancement in viscosity from 0.887 mPa s to 18.25 mPa s is achieved by adding glycerol to the aqueous solution of KCl while maintaining the conductivity identical to the base solution ($\sigma_s =$ 13.18 mS/cm). The experiments suggest that the overall dynamics of the aforementioned three stages remain very similar regardless of the viscosity of the droplet. The phenomenon initiates with a cohesive failure of the droplet due to discharge [see Figs. 11(a)–11(c)] before the formation and expansion of crown with a rim decorated with spikes [see Figs. 11(d)–11(g)] takes place. Such elongated spikes are characteristics of the Richtmyer-Meshkov instability, observed during large initial acceleration of a liquid sheet [88]. We also observe early ejection of liquid mass due to the breakup of some of these spikes via capillary instability of threads [see Figs. 11(e) and 11(f)].

The expansion of the crown up to approximately 0.9 ms also favors the formation of a rim, as shown in Figs. 11(d)–11(g). The unstable rim subsequently generates thick ligaments, which again undergo capillary breakup to generate secondary droplets during the expansion stage. The size of the secondary droplets generated by the stable viscous sheet ranges from 0.1 to 0.4 mm. Further, a quantitative analysis of the frames from early expansion stage of Fig. 11 indicates that the maximum velocity of expansion of the crown, $U_c^e$, is approximately 2.0 m/s. The sheet starts retracting at approximately 0.9 ms indicating the onset of the sealing and collapse stage, accompanied by the movement of the TPCL towards the anode, as shown in Figs. 11(h)–11(l) (refer to Movie 9 within the Supplemental Material [53]). Notably, this movement of the contact line is not prominent during the collapse of less viscous liquid sheets (refer to Fig. 10). However, such TPCL retraction for more viscous droplets favors the formation of a "necking region" below the thicker rim, as shown by the red circle and arrows in Figs. 11(k) and 11(l). Here, we observe a prolonged sealing and collapsing phase ($t_c \approx 0.8 t_{\text{sheet}} \approx 3$ ms), owing to the significant viscous resistance offered against the fluid motion for these activities. Although not shown in Fig. 11 (shown in Movie 9 within the Supplemental Material [53]), beyond 1.7 ms, the crown collapses progressively due to the influence of the surface-tension force [34].

It may be noted here that, neglecting any loss of liquid mass during the early expansion phase, the calculated velocity of crown expansion ($U_c^e$, is approximately 2.0 m/s) corresponds to an average kinetic energy of $2.01 \times 10^3$ mJ/kg, which is approximately 0.45% of the total discharge energy from the electric field. Thus, a strong viscous force confines more discharge energy to develop a more stable crown, as shown in Fig. 11. An increase in the magnitude of the viscosity ($\eta \sim O[10^{-3}] \rightarrow \eta \sim O[10^{-1}]$) of the droplet raises both Ca (approximately $O[10^0]$) and Oh (approximately $O[10^{-1}]$) by 2 orders of magnitude as compared to the less viscous case, which corroborates the dominant role of viscosity on the hydrodynamics and the presence of a kinetically controlled crown formation.

Figures 12(a) and12(c) show the contours of the outer wall of the liquid-air interface of the initial droplet and the crown after the electric discharge, extracted from the time-resolved images presented in Figs. 10 and 11, respectively. For the sake of brevity and clarity, we show only a half cross section of the droplet in the plots. Here, we use a set of different symbols, namely, circle, square, and triangle filled and bordered with black, blue, and green color, respectively, to depict the previously mentioned three distinct stages of crown dynamics with the help of contours. The plots, Figs. 12(a) and 12(c), suggest that in the post-discharge phase the crown grows in all three, radial ($r$), vertical ($z$), and azimuthal directions (considering the liquid sheet as a annular cylinder, the angular direction is termed as azimuthal, $\theta$). The contours in Fig. 12(c), distinctly exhibit the motion of TPCL for the highly viscous liquid sheet. The TPCL is forced to move away from the center of the droplet in the expansion phase, whereas it retracts itself back to the center in the sealing phase under the effect of surface-tension force. Interestingly, this kind of distinct contact line motion is absent in less viscous liquid sheet, as shown by the contour in Fig. 12(a). The various stages of crown dynamics can further be deciphered by the distinct change of slope in the trajectory of "neck radius," $r_c$ in Figs. 12(b) and 12(d). For example, the maximum value of the necking regime indicates the end of the expansion stage at 1.5 ms for the less viscous case. Also, for the high-viscosity droplet, we are not able to measure the neck radius beyond 1.7 ms as the neck merges with the rim, although it has a substantially larger time scale for the sealing and collapsing phase (approximately 3 ms) in comparison to the expansion phase.

### E. Bursting regime

Apart from the crown formation and jetting, the liquid droplets can also "burst" into numerous smaller ones under the influence of an intense electrical discharge. Notably, a droplet with higher electrical conductivity ($C_s \geq 0.5$ M) can promote such catastrophic "bursting" mode under a high-field-intensity discharge. Similar fragmentation of a droplet has previously been observed only for high-intensity pulsed laser or x-ray exposures [34,35,89].

Figure 13 (see also Movie 10 within the Supplemental Material [53]) shows the spatiotemporal evolution of the droplet during a discharge-mediated "bursting."

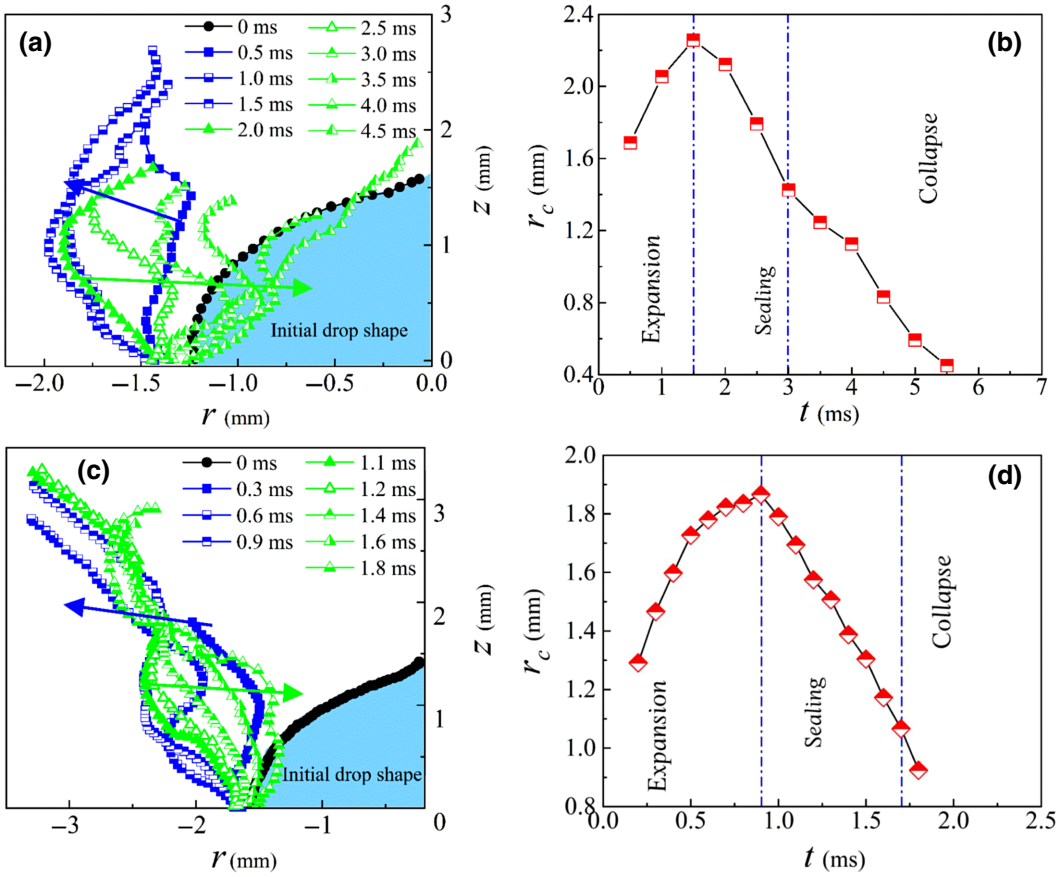


FIG. 12. Images (a),(c) represent the contour of the liquid-air interface of the crown for a low (Oh = 0.003) and a high (Oh = 0.056) viscosity droplet, respectively. Here, we use a set of different symbols, namely, circle, square, and triangle filled and bordered with black, blue, and green color, respectively, to depict the previously mentioned three distinct stages of crown evolution, namely, the droplet before electric discharge, the crown formation, and expansion, and finally the sealing and collapse of the crown, with the help of contours. The blue arrow pointing towards the left indicates the direction of expansion of the crown while the green arrow pointing rightward indicates the direction of crown sealing. Plots (b) and (d) show the rate of change of the neck radius, $r_c$, corresponding to the crown-formation events shown in Figs. 10 and 11, respectively.

The discharge is confined within a 5-$\mu$l droplet of 1 M KCl solution (solution 5, Table II) by applying a field of intensity, $\Psi = 60$ kV/cm, having a specific discharge energy, $E_d \approx 7.60 \times 10^5$ mJ/kg. Figures 13(a) and 13(b) show that in a timespan of $t < 1$ ms the discharge is translated into rapidly expanding cavitation bubbles, which

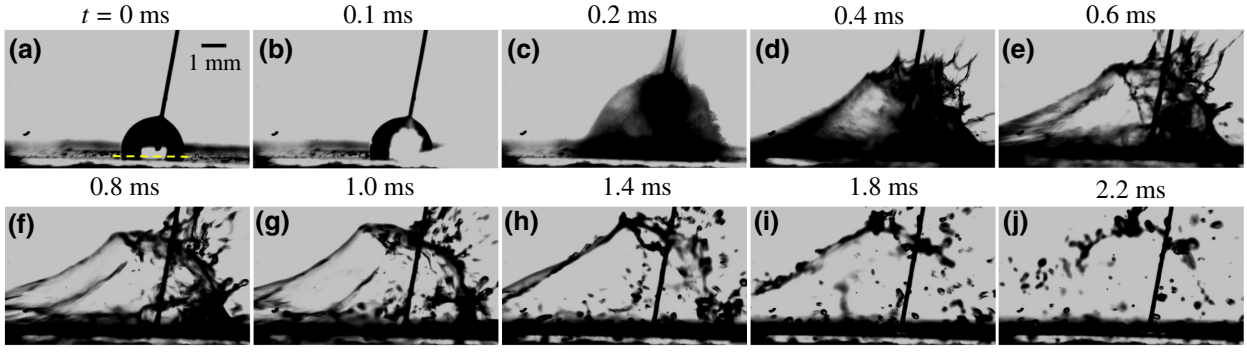


FIG. 13. The snapshots show the spatiotemporal evolution of a liquid drop of high electrical conductivity (1 M) and low viscosity ($\eta = 0.886$ mPa s) subjected to an electric field discharge. The other experimental parameters are $\psi = 1200$ V, $\Psi = 60$ kV/cm, and $V_{\text{drop}} = 5$ $\mu$l. The yellow broken line on image (a) shows the position of the datum. The frames are captured at a rate of 10 000 frames per second.

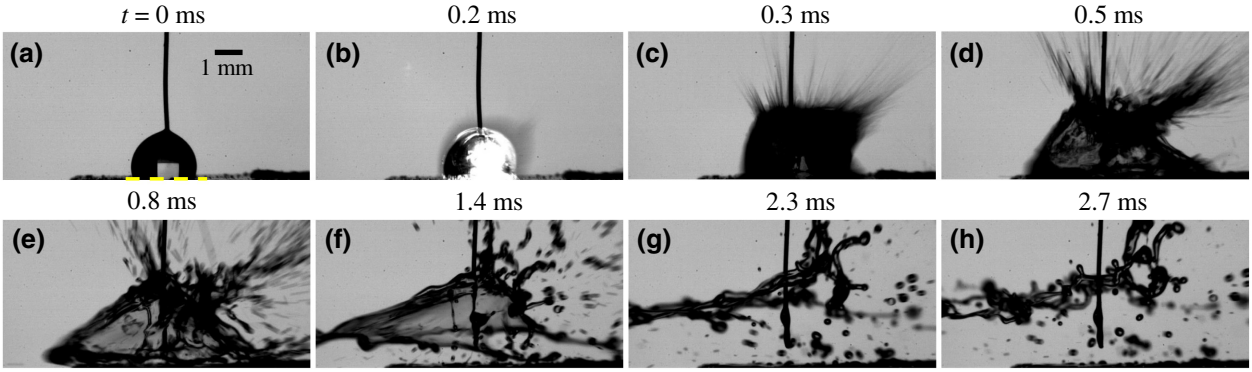


FIG. 14. The snapshots show the spatiotemporal evolution of a liquid drop of moderate viscosity (solution 6, Table II) and low electrical conductivity (0.1 M) subjected to an electric field discharge. The other experimental parameters are $\psi = 800$ V, $\Psi = 16$ kV/cm, and $V_{\text{drop}} = 5$ $\mu$l. The yellow broken line on the image (a) shows the position of the datum. The frames are captured at a rate of 10 000 frames per second.

in turn cause the bursting of the droplet, as shown in Fig. 13(c). The bursting is indicated by the production of a fine mist along with unstable liquid sheet(s), which eventually ejects an array of minuscule secondary droplets. The liquid sheet is also found to accelerate radially outward with an expansion velocity of approximately 20 m/s along with the formation of thin ligaments of fluid attached to a growing rim, as shown in Figs. 13(d) and 13(e). Figure 13(f) shows that the thin liquid sheet and fluid ligaments eventually rupture and eject secondary droplets of size ranging from 0.1 to 0.5 mm. After formation, the secondary droplets are ejected away radially at an average speed of approximately 4 m/s. The average kinetic energy of "bursting" is found to be approximately 1 mJ for this less viscous droplet of mass, $5.21 \times 10^{-6}$ kg, leading to an efficiency of approximately 27.5%.

Figure 14 (see also Movie 11 within the Supplemental Material [53]) shows the bursting dynamics of a moderately viscous liquid droplet (solution 6, Table II) at an applied field intensity of $\Psi = 16$ kV/cm. The initial dynamics of discharge generation and subsequent unstable sheet formation for the viscous droplets are analogous to the previously discussed less viscous (DI-water) case in Fig. 13. Briefly, for the moderately viscous case in Fig. 14, the liquid sheet moves radially outward at an (maximum) expansion velocity of approximately 10 m/s when the $E_d \approx 3.01 \times 10^5$ mJ/kg. Notably, the liquid spikes generated along the growing rim of the liquid sheet are more prominent in this case in comparison to the less-viscous situation. With the progress in time, the liquid droplets are ejected in the form of fine sprays from the sheet, while the liquid rim becomes much thicker, as shown in Figs. 14(b)–14(f). A larger viscous resistance also increases the lifetime of the unstable liquid sheet to 1.5 ms.

Subsequently, the unstable sheet collapses into the liquid rim [see Figs. 14(g) and 14(h)], which finally disintegrates into an array of secondary droplets undergoing a Plateau-Rayleigh instability, as seen for the less-viscous droplet. Considering the expansion velocity of approximately 10 m/s, we obtain a discharge efficiency approximately 18% in this case, while observing a complete disintegration of the parent droplet into secondary droplets with a size range of approximately 0.05–0.5 mm. Figure 15 and Movie 12 within the Supplemental Material [53] show the bursting dynamics of a high-viscosity liquid droplet (solution 9, Table II) at an applied field intensity of $\Psi = 18.9$ kV/cm, having $E_d \approx 1.09 \times 10^5$ mJ/kg. While the initial dynamics of sheet formation and breakup remain similar to the previous two cases (Figs. 13 and 14), the fluid ligaments are found to be prominent for a much longer period until 2.4 ms. The viscous resistance kinetically stabilizes the liquid sheet and the rim to delay the growth of large-scale perturbations and subsequent disintegration into the secondary droplets. Further, Figs. 13–15 suggest that the diameter of the fluid ligaments reduces with the increase in the viscosity of the liquid droplet. The discharge efficiency for the present scenario is found to be approximately 30% by considering the maximum expansion velocity of the liquid sheet approximately 9 m/s, and ignoring any early mass loss.

### F. Dynamics of microjetting

Apart from the jetting, crowning, and bursting of droplets, we also observe the formation of "microjets" in the postdischarge scenario, as shown in Fig. 16. Previously, Thoroddsen *et al.* [87] have reported the formation of microjets in the context of laser-droplet interaction, when the focal point of the laser pulse has been well inside the liquid phase. Figure 16(b) shows that confining an electric discharge in a droplet can also emanate such liquid jets from the top of the droplet, as marked by the yellow broken circle. Such jets are expected to form as a

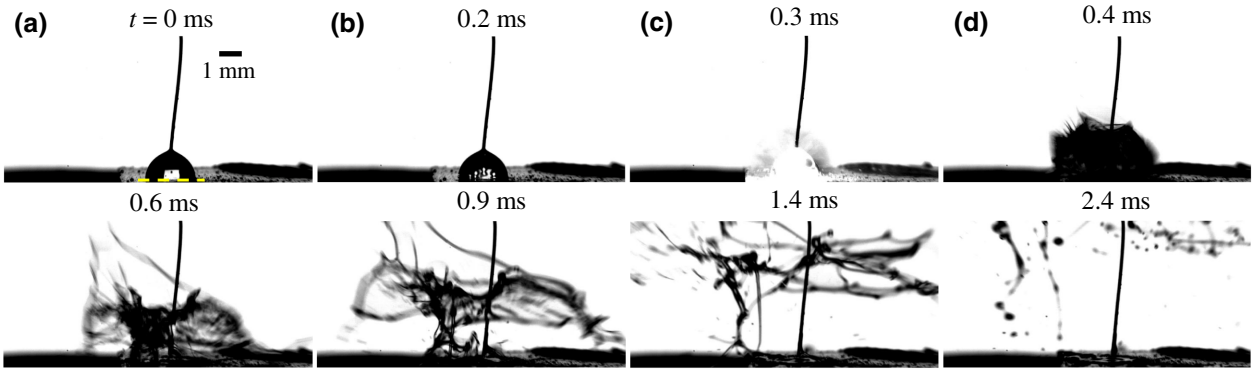


FIG. 15. The snapshots show the spatiotemporal evolution of a liquid drop of high viscosity (solution 9, Table II) and low electrical conductivity (0.1 M) subjected to an electric field discharge. The other experiment parameters are $\psi = 500$ V, $\Psi = 18.9$ kV/cm, and $V_{\text{drop}} = 5$ $\mu$l. The yellow broken line on the image (a) shows the position of the datum. The frames are captured at a rate of 10 000 frames per second.

result of the interaction of the preexisting thermal bubbles [see Fig. 16(a)] with the APWs immediately after discharge. This proposed mechanism can be backed by several experimental observations from the present study as well as drawing an analogy with the microjets reported by Thoroddsen *et al.* [87]. Firstly, these fine jets often emerge from the apex area of the liquid-air interface, where the probability of finding smaller bubbles is maximum [see Figs. 16(a) and 16(b)]. These preexisting bubbles act as nuclei of microjet generation after absorbing the energy of the high-pressure waves released during the discharge [refer to Fig. 16(b)]. As such the underlying mechanism of the generation of these microjets is markedly different from those regular jets discussed in Sec. III C, where the latter is produced by the pressure waves from the collapse of cavitation bubbles. Interestingly, these microjets disappear during discharge in a fresh droplet or if the bubbles are removed with a syringe prior to discharge [87]. Although we show the development of one single microjet in Figs. 16(a)–16(f), they can appear in large numbers, as shown in Fig. 16(g), from a more viscous droplet (solution 6 Table II). The experiments uncover that the velocity of such microjets ranges from 5 to 30 m/s, where the velocities of the viscous jets are comparatively higher. Further these microjets can generate droplets as small as 10 $\mu$m. In a way, the APW-mediated microjets contribute towards the effective atomization of the droplets during dielectric discharge. A detailed characterization of these microjets with the help of experiments is kept as future scope of research.

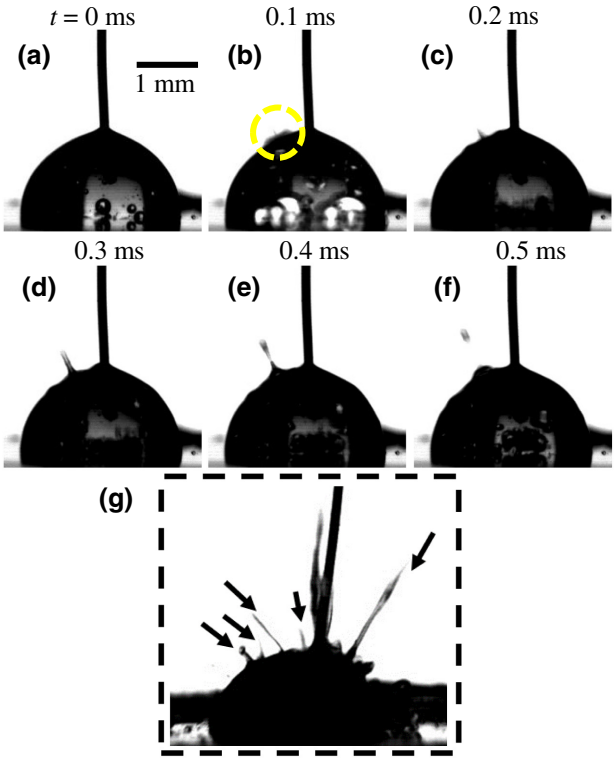


FIG. 16. (a)–(f) Dynamics of microjetting for a DI-water droplet (solution 3, Table II). The yellow broken circle in image (b) indicates the incipience of jet formation. (g) Dynamics of microjetting for a droplet of glycerol (50%)-water (50%) mixture (solution 6, Table II).

### G. Characterization of hydrodynamics

#### *1. Effects of electric field intensity and salt concentration*

Figure 17 shows the possibility of different electric-discharge-induced flow morphologies, namely, "jetting" (square, red), "crown formation" (circle, blue+cyan), "bursting" (triangle, olive), and "jetting + bursting" (diamond, purple), with the variation in the electric field intensity, expressed in terms of the electric Bond number (Bo) and the molar concentration of KCl in the solutions ($C_s$). Here "jetting+bursting" is the mixed regime, where both the phenomena are observed during discharge cycles.

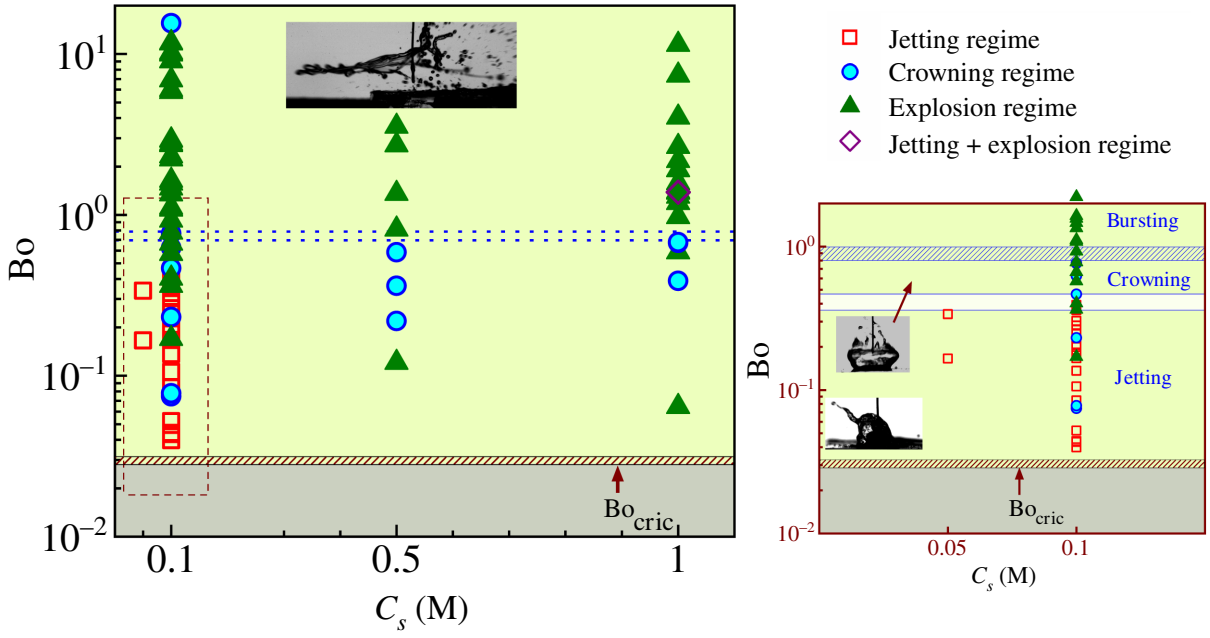


FIG. 17. Different regimes of electric-discharge-induced droplet atomization, namely, jetting (square, red), crown formation (circle, blue+cyan), bursting (triangle, olive), and jetting + bursting (diamond, purple) with the variation in the electric field intensity, expressed in terms of the electric Bond number (Bo) and the molar concentration of KCl in the droplet ($C_s$). The rectangular dashed region marked is shown in an enlarged view in the right-hand-side plot. The approximate borders are indicated with broken lines.

The plot suggests that for Bo $> 0.7$, the droplet undergoes "bursting" at all concentrations, as indicated by the blue dashed line. Further, the propensity of droplet bursting at lower electric fields, Bo $< 0.7$, increases with the salt concentration beyond 0.1 M. In contrast, a lower salt concentration ($C_s < 0.1$ M) and field intensity (Bo $< 0.35$) is seen to favor "jetting" phenomena. The regimes can be understood clearly from the right-hand-side plot, which is the enlarged view of the dashed rectangular regime.

Further, in the intermediate field intensity, $0.35 <$ Bo $< 0.7$, the "crown-formation" regime can be seen at 0.1, 0.5, and 1.0 M salt loading. For 0.1-M concentration, the transition from "crowning" to "bursting" is marked by a dashed rectangular zone, while the transition from "jetting" to "crowning" is marked by a white-colored regime in the right-hand-side plot. The plot also shows that for $C_s = 0.1$ M, all the flow morphologies can be obtained simply by tuning the electric field intensity, $\Psi$ (or Bond number, Bo), while keeping other parameters constant. The plot also highlights that the drops with 0.1-M salt loading may show all the flow morphologies with the variation in the electric field intensity (or Bo), whereas the droplets with more than 0.5-M salt are akin to bursting only. We also observe that all the phenomena are absent below Bo $= 0.032$ ($\Psi \leq 3$ kV/cm), which ensures the necessity of a critical electric field intensity ($\Psi_{cric}$ or critical bond number, $Bo_{cric}$) to cause the dielectric breakdown of the PDMS layer and subsequent electric discharge. The shaded brown regime marks the boundary of $Bo_{cric}$ for different experimental fluids, which is obtained with the help of control experiments. Furthermore, for the experimental solution with salt concentration, $C_s = 0.01$ M (solution 1, Table II), none of the discussed hydrodynamic features are observed within the range of electric potential studied herein. Instead, the droplet with the aforementioned conductivity exhibited general EWOD dynamics, which further illustrates the role of solution conductivity in the dielectric-discharge-induced droplet-deformation process.

### *2. Effect of the position of occurrence of electric discharge*

Apart from the electrical conductivity, viscosity, and field intensity, we observe that the position of occurrence of the electric discharge is another parameter, which influences the formation of a liquid-jet (A), liquid-crown (B), or bursting (C) phenomena, as shown in Fig. 18. For this purpose, initially, the best 30 experiments are selected in which the geometric center of the droplet and the center of the discharge are identified from the experimental snapshots, along $x$ and $z$ axes, with the help of the image-processing software ImageJ [58]. Thereafter, the normalization of the distances is done by the radius of the droplet prior to discharge ($r_d$). Combining all these parameters into the dimensionless parameters in space ($\delta_x, \delta_z$), each of the performed experiments has been assigned to one of the three categories ("A," "B," or "C"), as shown

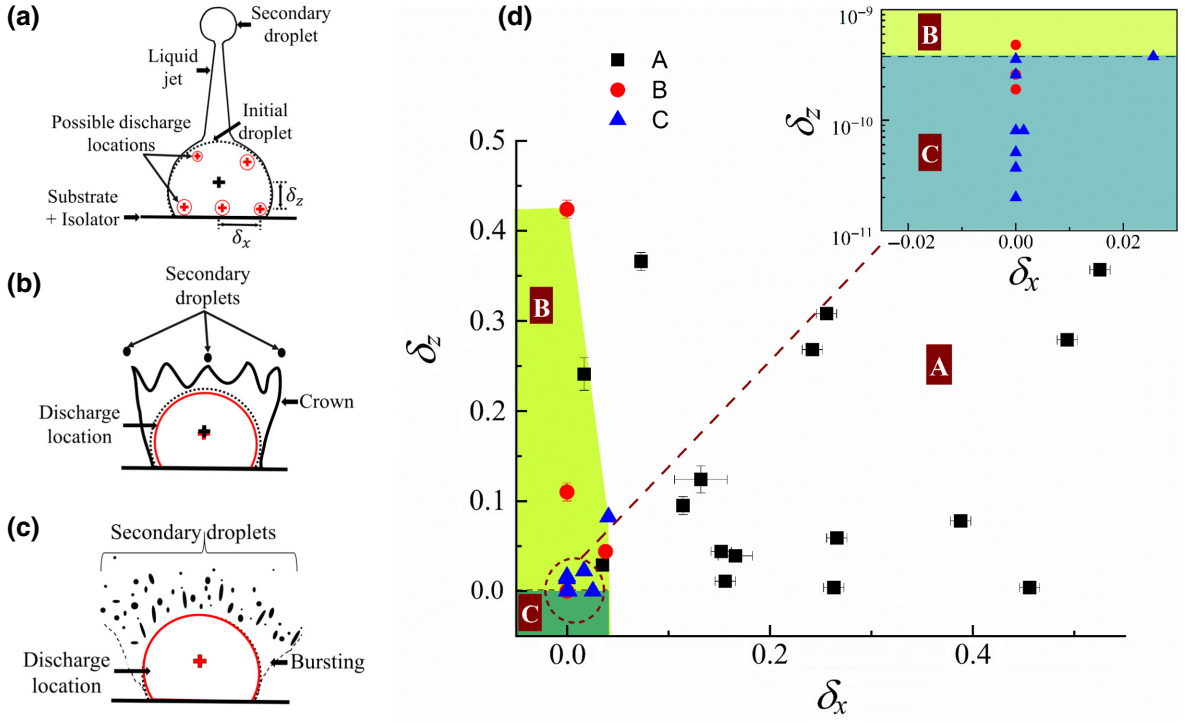


FIG. 18. Schematics (a)–(c) show the different locations of electric field discharge observed (zone with a red circle with a "+" sign at the center) with respect to the geometric center of the droplet (zone with a black circle with a "+" sign at the center) during the experiments. The dimensionless distance between these two points in the vertical and horizontal planes are denoted as $\delta_z$, and $\delta_x$, respectively. The plot (d) shows the occurrence of liquid jetting (A), crown formation (B), and bursting (C) in the $(\delta_x, \delta_z)$ plane. The broken line between the regions "B" and "C" divides the two regimes. The error bars are due to the uncertainty in determining the center for both the electric discharge and droplet. The red broken circle marks the area shown in the inset.

in Fig. 18. Figures 18(a)–18(c) schematically depict the probable positions of the electric field discharge observed (zone with a red circle with a "+" sign at the center) during the experiment with respect to the geometric center of the droplet (zone with a black circle with a "+" sign at the center). The normalized distance between these two points in the vertical and horizontal planes are denoted as $\delta_z$ and $\delta_x$, respectively. The experimental results suggest that a superimposition of the electric-field-discharge center and the geometric center of the droplet always results in the formation of the crown or bursting. In contrast, the deviations in the locations of discharge from the geometrical center of the droplet lead to the jetting phenomenon. The probability of jetting is enhanced with the increase in the distance between the discharge and the droplet center in either direction, as shown in Fig. 18(a), where the probable discharge locations are marked with a red circle. The aforementioned claim can be correlated with the multiple discharge hotspots along the electrodes, as discussed previously in Secs. III A and III B. The region $\delta_x > 0.035$ is found to be the possible region of jetting dynamics, while for the region $0 < \delta_x \leq 0.035$, it is difficult to distinguish between the crown formation and droplet bursting, as shown by the inset.

### H. Comparison with existing methods and target applications

In the current study, the sessile droplet exhibited the formation of liquid jets when exposed to a lower intensity discharge. Similar studies have been carried out in the recent past to engender liquid jet from a free surface initially at rest by creating overpressure at the jet base. In this regard, Fletcher and Palanker [31] report the formation of liquid jets created by electric discharge induced vapor bubble, which is then successfully used for incision of soft tissues. The study suggests that a jet of 30 $\mu$m diameter can reach a velocity of 90 m/s at an energy conversion efficiency of approximately 10%, about an order of magnitude higher than the one we propose here. Similarly, Avila *et al.* [90] have shown the formation of high-speed microjets mediated by the spark-induced cavitation bubble at an efficiency of approximately 2%–5%, much closer to the efficiency reported by us (approximately 0.35%–2%). Further, Tan *et al.* [91] could form liquid jets by accelerated Rayleigh waves, while Tomita [92] has shown the characteristics of the jetting using an ultrasound source of intensity, $I = 220$ W/cm$^2$ with an exposure time of 3–5 ms, at an efficiency of $< 1\%$. Notably, the velocity of the liquid jets reported by the latter study (0.48–2.2 m/s) matches

TABLE III. Comparison between the current study and recent experimental studies for liquid-jet generation.

| Study | Method of jet generation | Velocity (m/s) | Kinetic energy ($\mu$J) |
|---|---|---|---|
| Tomita [92] | Ultrasound | 0.48–2.2 | ~0.02–0.08 |
| Avila *et al.* [90] | Spark energy | up to 400 | up to 15 |
| Delrot *et al.* [101] | Laser pulse | 4–7 | NA |
| Onuki *et al.* [102] | Impulsive force | 2–15 | NA |
| Current study | Dielectric discharge energy | 1.5–4.8 | 1.35–11 |

closely to that of ours (see Table III). Apart from the above examples, several other studies have reported the dynamics of the liquid jets emanating from a free surface by using pulsed laser [28,69], shock waves [32,64], or blast waves [93]. In Table III, we further compare the jetting events of this study with a few recent literatures, wherein the reported jet velocity or the kinetic energy is much closer to that of the former. Notably, the creation of overpressure beneath the free surface enables liquid jetting in the absence of nozzles or any liquid reservoirs as discussed above, which is in stark contrast to the jetting observed in electrospinning, electrospraying, or in gas dynamic virtual nozzles (GDVN) [94–100]. Also, the latter methods [94–100] have been used extensively for continuous production of secondary droplets from an emerging liquid jet, unlike the proposed method.

The prior art also reports that the dielectric breakdown of a liquid can lead to interesting hydrodynamic features such as jet, counter jet, crown, ejecta sheet, or plumes, to name a few [8,28,34,87,103]. In this regard, Obreschkow *et al.* [28] have reported that the confinement of an electric-spark-induced cavitation bubble inside a centimetric droplet can produce jets, counter jet, and splash, which is similar to that of our study. The study shows that the microjet speed can go beyond 50 m/s with an efficiency of 30%–50%. On a similar note, a disruption efficiency of $>$ 30% for the bursting mode has also been discussed for the present study. Further, Thoroddsen *et al.* [87] have studied the formation of spray and microjets from sessile liquid droplets mediated by intense 30 mJ/pulse laser energy for approximately 7 ns. They report that the tip of the disruption sheet can acquire a speed of approximately 1400 m/s leading to the formation of "laser crown" at an efficiency of approximately 20%, again similar to that of the present study. Furthermore, Avila and Ohl [34] have reported the fragmentation of acoustically levitated water droplets exposed to a single laser-induced cavitation bubble. The dynamics of the "rapid atomization" and the "unstable sheet formation" regime mentioned there has a striking similarity with the "bursting mode" discussed in this study. The corresponding energy conversion efficiency (laser energy $\rightarrow$ bubble energy) is approximately 0.35% for the rapid atomization mode and approximately 7% for the "coarse fragmentation regime," as shown in the study. Again, the "stable sheet fragmentation mode" has similar dynamics to that of the crown-formation regime in our study, which can have an energy efficiency of nearly 1%–3% [34], a value close to ours. Interestingly, Vogel *et al.* [103] have previously reported the maximum energy conversion efficiency of 10% for nanosecond laser pulses. Furthermore, Klein *et al.* have observed drop deformation and fragmentation by using a plasma propulsion tool to accelerate the flow in a levitated liquid droplet [8,104], a setup specifically designed for EUV nanolithography applications. In another unique study, James *et al.* [42] have reported the formation of a polydisperse spray from a sessile droplet of volume 100 $\mu$l due to its exposure to substrate vibration near resonance.

Thus, from the aforementioned discussion, it is apparent that the efficiencies of the various processes reported for the present method are rather competitive if not similar or superior to the processes available so far. However, such comparative studies are to be explored under the perspective of the difference in the underlying mechanisms involved with the methodologies associated with light, sound, electric field, or others.

## IV. CONCLUSIONS

In summary, we confine an electric discharge phenomenon in a liquid microdroplet to study the time-resolved EHD. The major conclusions are as follows.

1. Emulating an EWOD setup, the droplet on a cathode-isolator pair is integrated with an anode from the top to confine the discharge in the liquid. Beyond a critical field intensity, the dielectric breakdown generates a discharge in the form of releasing localized light and/or thermal energies, which in turn causes actuation, expansion, and collapse of cavitation bubbles in the droplet. Subsequently, several discharge-mediated bursting, jetting, and crown formation, have been observed. The crowns are characterized by the formation of a metastable cylindrical liquid sheet topped by a developed rim decorated with periodic liquid spikes. On the other hand, the liquid jets show an upward movement before breaking into an array of secondary droplets. Further, in comparison to the previously reported laser-based setups [8], we show a simpler, as well as economic (in terms of the mechanical energy conversion efficiency) alternative of "bursting" of a droplet

into an array of microdroplets in a few milliseconds [87]. Conditionally, we also observe some interesting flow morphologies, which include high-aspect-ratio microjets, end pinching of a liquid jet, high-aspect-ratio liquid spikes riding on the rim of a crown, and capillary breakup of a liquid jet, among others. The energy conversion efficiency of bursting is found to be approximately 25%–30%, while the same has been less than 2% for the jetting or crown formation.

2. The simulations uncover that the location of dielectric breakdown under the droplet can be one of the relevant factors for developing different flow morphologies. For example, a bursting phenomenon can be expected at high field intensity when the breakdown is immediately under the anode (i.e., at the center of the droplet base). In contrast, jetting (crowning) can be observed at lower (intermediate) field intensities when the breakdown takes place near the three-phase contact line of the droplet. The deviation of the discharge location from the center of gravity of the droplet is another factor that is found to decide the type of flow morphology observed after discharge. Interestingly, the transition of flow morphologies can be done by tuning the thermodynamic factors such as the applied electric field intensity and/or the droplet size and the kinetic parameters such as the electrical conductivity and/or viscosity of the droplet. While a higher electrical conductivity ($\geq$ 0.5 M) and field intensity ($>$15 kV/cm) facilitate bursting, a lower field intensity leads to the crown formation or jetting. Again, for a given field intensity and conductivity, different flow morphologies can be obtained by tuning the viscosity of the droplet. The theoretical and experimental time scales for the discharge-mediated formation and sealing of crown, formation, and the breakup of a jet, and bursting of the droplet are discussed based on the balances of the electric field, surface tension, and the viscous forces.

3. During the jetting, in the front, the bulbous secondary droplet is formed following the well-known "end-pinching" mechanism [76] while the rest of the jet breaks following the "Plateau-Rayleigh instability" (primarily in the case of viscous jets). About five- to tenfold miniaturization of the primary droplet is observed during such a process. In contrast, the bursting of the droplet leads to approximately 30- to 40-fold miniaturization, highlighting the potential of the proposed method in the development of liquid sprays or atomizers.

4. The droplet atomization strategy proposed here is competitive, if not similar or superior, to the processes available, in terms of energy efficiency. However, such comparative studies are to be explored considering the difference in underlying mechanisms involving light, sound, electric, or magnetic fields. Also, the overall efficiency of the current method is to be compared and contrasted against some of the commonly employed droplet atomization techniques [94–100]. In the near future, alongside exploring the fundamental and applied aspects of the proposed phenomenon, the applications of the same for inkjet printing [27], electrospraying [50], droplet miniaturization, tissue ablation [51], electroporation [52], or biomedical devices [31] can also be explored.

## ACKNOWLEDGMENTS

We thank DST SERB, Grant No. EMR/2016/001824, MeitY, Grant No. 5(9)/2012-NANO, and the DST-FIST-grant SR/FST/ETII-028/2010, Government of India, for financial support.

[1] M. A. Uman, *The Lightning Discharge* (Dover Publications, New York, 2001).
[2] J. M. Meek, A theory of spark discharge, Phys. Rev. **57**, 722 (1940).
[3] S. R. Mahmoudi, K. Adamiak, and G. S. P. Castle, Spreading of a dielectric droplet through an interfacial electric pressure, Proc. R. Soc. A **467**, 3257 (2011).
[4] G. Xie, F. He, X. Liu, L. Si, and D. Guo, Sessile multidroplets and salt droplets under high tangential electric fields, Sci. Rep. **6**, 25002 (2016).
[5] A. E. Dubinov, J. P. Kozhayeva, V. V. Golovanov, and V. D. Selemir, Coalescence of liquid droplets under effect of pulsed-periodic spark discharges, IEEE Trans. Plasma Sci. **47**, 76 (2018).
[6] J. F. Waymouth, *Electrical Discharge Lamps* (MA: MIT Press, Cambridge, 1971).
[7] J. M. Grace and J. C. M. Marijnissen, A review of liquid atomization by electrical means, J. Aerosol Sci. **25**, 1005 (1994).
[8] A. L. Klein, W. Bouwhuis, C. W. Visser, H. Lhuissier, C. Sun, J. H. Snoeijer, E. Villermaux, D. Lohse, and H. Gelderblom, Drop Shaping by Laser-Pulse Impact, Phys. Rev. Appl. **3**, 044018 (2015).
[9] B. Sarma, V. Shahapure, A. Dalal, and D. N. Basu, Magnetowetting dynamics of sessile ferrofluid drops on soft surfaces, Soft. Matter. **16**, 970 (2020).
[10] H. N. Oguz and A. Prosperetti, Bubble entrainment by the impact of drops on liquid surfaces, J. Fluid Mech. **219**, 143 (1990).
[11] A. L. Yarin, Drop impact dynamics: Splashing, spreading, receding, bouncing, Annu. Rev. Fluid Mech. **38**, 159 (2006).
[12] I. T. Adebayo and O. K. Matar, Droplet impact on flowing liquid films with inlet forcing: The splashing regime, Soft. Matter. **13**, 7473 (2017).
[13] A. M. Worthington, On the forms assumed by drops of liquids falling vertically on a horizontal plate, Proc. R. Soc. Lond. 25, 261 (1876).
[14] A. M. Worthington, *A Study of Splashes* (Longmans, Green, and Company, London, 1908).
[15] A. May, Vertical entry of missiles into water, J. Appl. Phys. **23**, 1362 (1952).
[16] M. Versluis, High-speed imaging in fluids, Exp. Fluids **54**, 1458 (2013).

[17] J. O. Marston, T. T. Truscott, N. B. Speirs, M. M. Mansoor, and S. T. Thoroddsen, Crown sealing and buckling instability during water entry of spheres, J. Fluid Mech. **794**, 506 (2016).

[18] Z. Che and O. K. Matar, Impact of droplets on liquid films in the presence of surfactant, Langmuir **33**, 12140 (2017).

[19] B. E. Scharfman, A. H. Techet, J. W. M. Bush, and L. Bourouiba, Visualization of sneeze ejecta: Steps of fluid fragmentation leading to respiratory droplets, Exp. Fluids **57**, 24 (2016).

[20] S. Tomotika, On the instability of a cylindrical thread of a viscous liquid surrounded by another viscous fluid, Proc. R. Soc. Lond. A **150**, 322 (1935).

[21] E. Villermaux and B. Bossa, Single-drop fragmentation determines size distribution of raindrops, Nat. Phys. **5**, 697 (2009).

[22] P. Roach, N. J. Shirtcliffe, and M. I. Newton, Progess in superhydrophobic surface development, Soft. Matter. **4**, 224 (2008).

[23] S. Timung, J. Chaudhuri, M. P. Borthakur, T. K. Mandal, G. Biswas, and D. Bandyopadhyay, Electric field mediated spraying of miniaturized droplets inside microchannel, Electrophoresis **38**, 1450 (2017).

[24] V. Yang and W. Anderson, *Liquid Rocket Engine Combustion Instability* (DC: AIAA, Washington, 1995).

[25] N. Lad, A. Aroussi, and M. F. Muhamad Said, Droplet size measurement for liquid spray using digital image analysis technique, J. Appl. Sci **11**, 1966 (2011).

[26] C. Priest, A. Quinn, A. Postma, A. N. Zelikin, J. Ralston, and F. Caruso, Microfluidic polymer multilayer adsorption on liquid crystal droplets for microcapsule synthesis, Lab. Chip **8**, 2182 (2008).

[27] S. D. Hoath, *Fundamentals of Inkjet Printing: the Science of Inkjet and Droplets* (John Wiley & Sons, New York, 2016).

[28] D. Obreschkow, P. Kobel, N. Dorsaz, A. de Bosset, C. Nicollier, and M. Farhat, Cavitation Bubble Dynamics inside Liquid Drops in Microgravity, Phys. Rev. Lett. **97**, 094502 (2006).

[29] G. E. Cossali, M. Marengo, and M. Santini, Thermally induced secondary drop atomisation by single drop impact onto heated surfaces, Int. J. Heat Fluid Flow **29**, 167 (2008).

[30] T. Kodama and Y. Tomita, Cavitation bubble behavior and bubble–shock wave interaction near a gelatin surface as a study of in vivo bubble dynamics, Appl. Phys. B **70**, 139 (2000).

[31] D. A. Fletcher and D. V. Palanker, Pulsed liquid microjet for microsurgery, Appl. Phys. Lett. **78**, 1933 (2001).

[32] B. Karri, S. W. Ohl, E. Klaseboer, C. D. Ohl, and B. C. Khoo, Jets and sprays arising from a spark-induced oscillating bubble near a plate with a hole, Phys. Rev. E **86**, 036309 (2012).

[33] J. O. Marston, M. M. Mansoor, S. T. Thoroddsen, and T. T. Truscott, The effect of ambient pressure on ejecta sheets from free-surface ablation, Exp. Fluids **57**, 61 (2016).

[34] S. R. G. Avila and C. D. Ohl, Fragmentation of acoustically levitating droplets by laser-induced cavitation bubbles, J. Fluid Mech. **805**, 551 (2016).

[35] C. A. Stan, D. Milathianaki, H. Laksmono, R. G. Sierra, T. A. McQueen, M. Messerschmidt, G. J. Williams, J. E. Koglin, T. J. Lane, M. J. Hayes, and S. A. Guillet, Liquid explosions induced by $X$-ray laser pulses, Nat. Phys. **12**, 966 (2016).

[36] C. Janzen, R. Fleige, R. Noll, H. Schwenke, W. Lahmann, J. Knoth, P. Beaven, E. Jantzen, A. Oest, and P. Koke, Analysis of small droplets with a new detector for liquid chromatography based on laser-induced breakdown spectroscopy, Spectrochim. Acta B **60**, 993 (2005).

[37] V. Y. Banine, K. N. Koshelev, and G. H. P. M. Swinkels, Physical processes in euv sources for microlithography, J. Phys. D **44**, 253001 (2011).

[38] I. Apitz and A. Vogel, Material ejection in nanosecond Er:Yag laser ablation of water, liver, and skin, Appl. Phys. A **81**, 329 (2005).

[39] T. C. de Goede, N. Laan, K. G. de Bruin, and D. Bonn, Effect of wetting on drop splashing of newtonian fluids and blood, Langmuir **34**, 5163 (2017).

[40] B. Ray, G. Biswas, and A. Sharma, Oblique drop impact on deep and shallow liquid, Commun. Comput. Phys. **11**, 1386 (2012).

[41] J. M. Kolinski, L. Mahadevan, and S. M. Rubinstein, Drops can bounce from perfectly hydrophilic surfaces, Europhys. Lett. **108**, 24001 (2014).

[42] A. J. James, B. Vukasinovic, M. K. Smith, and A. Glezer, Vibration-induced drop atomization and bursting, J. Fluid Mech. **476**, 1 (2003).

[43] A. Antkowiak, N. Bremond, S. Le Dizès, and E. Villermaux, Short-term dynamics of a density interface following an impact, J. Fluid Mech. **577**, 241 (2007).

[44] D. Bartolo, C. Josserand, and D. Bonn, Singular Jets and Bubbles in Drop Impact, Phys. Rev. Lett. **96**, 124501 (2006).

[45] L. V. Zhang, P. Brunet, J. Eggers, and R. D. Deegan, Wavelength selection in the crown splash, Phys. Fluids **22**, 122105 (2010).

[46] H. Lhuissier and E. Villermaux, Bursting bubble aerosols, J. Fluid Mech. **696**, 5 (2012).

[47] D. Fuster, G. Agbaglah, C. Josserand, S. Popinet, and S. Zaleski, Numerical simulation of droplets, bubbles and waves: State of the art, Fluid Dyn. Res. **41**, 065001 (2009).

[48] F. Mugele and J. C. Baret, Electrowetting: From basics to applications, J. Phys. Condens. Matter **17**, R705 (2005).

[49] S. Kumar, B. Sarma, A. K. Dasmahapatra, A. Dalal, D. N. Basu, and D. Bandyopadhyay, Field induced anomalous spreading, oscillation, ejection, spinning, and breaking of oil droplets on a strongly slipping water surface, Faraday Discuss. **199**, 115 (2017).

[50] H. Li, Y. Gan, X. Chen, Y. Tong, and M. Hu, in *Experimental Study on Electro-Spraying of Ethanol Based on PDA Measurement. Energy Technology, The Minerals, Metals & Materials Series* (Springer, Cham., 2017).

[51] B. I. Lee, E. R. Rodriguez, A. Notargiocomo, V. J. Ferrans, Y. Chen, and R. D. Fletcher, Thermal effects of laser and electrical discharge on cardiovascular tissue: Implications for coronary artery recanalization and endocardial ablation, J. Am. Coll. Cardiol. **8**, 193 (1986).

[52] H. Potter and R. Heller, Transfection by electroporation, Curr. Protoc. Mol. Biol. **121**, 9 (2018).

[53] See Supplemental Material at http://link.aps.org/supplemental/10.1103/PhysRevApplied.15.014005 for additional information on energy efficiency, robustness, and repeatability of the proposed method; ITO substrate cleaning procedure; effect of contact angle; comparison of different energy terms; numerical simulation method; viscous jet instability analysis; and Supplemental Videos.

[54] L. S. Tan and J. E. Mark, *Polymer Data Handbook* (Oxford University Press, NewYork, 1999).

[55] S. Krishnan, Ph.D. thesis, Massachusetts Institute of Technology, 2007.

[56] D. E. Goldsack and R. Franchetto, The viscosity of concentrated electrolyte solutions. i. concentration dependence at fixed temperature, Can. J. Chem **55**, 1062 (1977).

[57] P. Leroy, A. Lassin, M. Azaroual, and L. André, Predicting the surface tension of aqueous 1: 1 electrolyte solutions at high salinity, Geochim. Cosmochim. Acta **74**, 5427 (2010).

[58] C. A. Schneider, W. S. Rasband, and K. W. Eliceiri, NIH Image to ImageJ: 25 years of image analysis, Nat. Methods **9**, 671 (2012).

[59] R. Sarathi and G. Nagesh, UHF technique for identification of discharges initiated by liquid droplet in epoxy nanocomposite insulation material under ac voltages, J. Phys. D: Appl. Phys. **41**, 155407 (2008).

[60] T. Schultz, M. Pfeiffer, and C. M. Franck, Optical investigation methods for determining the impact of rain drops on HVDC corona, J. Electrostat. **77**, 13 (2015).

[61] U. Kogelschatz, Dielectric-barrier discharges: Their history, discharge physics, and industrial applications, Plasma Chem. Plasma Process. **23**, 1 (2003).

[62] T. C. Corke, C. L. Enloe, and S. P. Wilkinson, Dielectric barrier discharge plasma actuators for flow control, Annu. Rev. Fluid Mech. **42**, 505 (2010).

[63] B. Shapiro, H. Moon, R. L. Garrell, and C.-J. Kim, Equilibrium behavior of sessile drops under surface tension, applied external fields, and material variations, J. Appl. Phys. **93**, 5794 (2003).

[64] B. Karri, K. S. Pillai, E. Klaseboer, S. W. Ohl, and B. C. Khoo, Collapsing bubble induced pumping in a viscous fluid, Sens. Actuators A Phys. **169**, 151 (2011).

[65] H. M. Jones and E. E. Kunhardt, Pulsed dielectric breakdown of pressurized water and salt solutions, J. Appl. Phys. **77**, 795 (1995).

[66] P. K. Watson, Electrostatic and hydrodynamic effects in the electrical breakdown of liquid dielectrics, IEEE Trans. Electr. Insul. **2**, 395 (1985).

[67] J. P. Padilla-Martinez, J. C. Ramirez-San-Juan, N. Korneev, D. Banks, G. Aguilar, and R. Ramos-Garcia, Breaking the rayleigh-plateau instability limit using thermocavitation within a droplet, At. Sprays **23**, 487 (2013).

[68] W. Lauterborn, T. Kurz, R. Mettin, and C. D. Ohl, in *Advances in Chemical Physics*, edited by I. Prigogine and S. A. Rice (John Wiley & Sons, New York, 1999), Vol. 110, p. 295.

[69] E. Robert, J. Lettry, M. Farhat, P. A. Monkewitz, and F. Avellan, Cavitation bubble behavior inside a liquid jet, Phys. Fluids **19**, 067106 (2007).

[70] A. Shima, Studies on bubble dynamics, Shock Waves **7**, 33 (1997).

[71] L. Rayleigh, On the pressure developed in a liquid during the collapse of a spherical cavity, Phil. Mag. **34**, 94 (1917).

[72] M. A. Bruning, M. Costalonga, J. H. Snoeijer, and A. Marin, Turning Drops Into Bubbles: Cavitation by Vapor Diffusion through Elastic Networks, Phys. Rev. Lett. **123**, 214501 (2019).

[73] B. Han, K. Köhler, K. Jungnickel, R. Mettin, W. Lauterborn, and A. Vogel, Dynamics of laser-induced bubble pairs, J. Fluid Mech. **771**, 706 (2015).

[74] B. Vukasinovic, M. K. Smith, and A. Glezer, Mechanisms of free-surface breakup in vibration-induced liquid atomization, Phys. Fluids **19**, 012104 (2007).

[75] D. V. Palanker, D. A. Fletcher, J. Miller, P. Huie, M. Marmor, and M. S. Blumenkranz, Pulsed liquid microjet for intravascular injection, Proc. SPIE Opt. Technol. 4611, 72 (2002).

[76] H. A. Stone, B. J. Bentley, and L. G. Leal, An experimental study of transient effects in the breakup of viscous drops, J. Fluid Mech. **173**, 131 (1986).

[77] J. Eggers and E. Villermaux, Physics of liquid jets, Rep. Prog. Phys. **71**, 036601 (2008).

[78] L. Rayleigh, On the capillary phenomena of jets, Proc. R. Soc. London **29**, 71 (1879).

[79] F. D. Rumscheidt and S. G. Mason, Break-up of stationary liquid threads, J. Colloid Sci. **17**, 260 (1962).

[80] W. K. Lee and R. W. Flumerfelt, Instability of stationary and uniformly moving cylindrical fluid bodies–i. newtonian systems, Int. J. Multiph. Flow **7**, 363 (1981).

[81] G. H. McKinley, Dimensionless groups for understanding free surface flows of complex fluids, Soc. Rheol. Bull. **74**, 6 (2005).

[82] S. Chandrasekhar, *Hydrodynamic and Hydromagnetic Stability* (Oxford University Press, London, 1961).

[83] J. W. M. Bush, *18.357 Interfacial Phenomena*, MIT OpenCourseWare, https://ocw.mit.edu. License: Creative Commons BY-NC-SA (Massachusetts Institute of Technology, Cambridge, United States, 2010).

[84] A. M. Worthington and R. S. Cole, Impact with a liquid surface studied by the aid of instantaneous photography. paper II, Phil. Trans. R. Soc. Lond. A **194**, 175 (1900).

[85] D. C. K. Rao and S. Karmakar, Crown formation and atomization in burning multi-component fuel droplets, Exp. Therm. Fluid Sci. **98**, 303 (2018).

[86] G. Taylor, The instability of liquid surfaces when accelerated in a direction perpendicular to their planes. i, Proc. R. Soc. Lond. A **201**, 192 (1950).

[87] S. T. Thoroddsen, K. Takehara, T. G. Etoh, and C. D. Ohl, Spray and microjets produced by focusing a laser pulse into a hemispherical drop, Phys. Fluids **21**, 112101 (2009).

[88] R. Krechetnikov and G. M. Homsy, Crown-forming instability phenomena in the drop splash problem, J. Colloid Interface Sci. **331**, 555 (2009).

[89] P. I. Singh and C. J. Knight, Pulsed laser-induced shattering of water drops, AIAA J. **18**, 96 (1980).

[90] S. R. G. Avila, C. Song, and C.-D. Ohl, Fast transient microjets induced by hemispherical cavitation bubbles, J. Fluid Mech. **767**, 31 (2015).

[91] M. K. Tan, J. R. Friend, and L. Y. Yeo, Interfacial Jetting Phenomena Induced by Focused Surface Vibrations, Phys. Rev. Lett. **103**, 024501 (2009).

[92] Y. Tomita, Jet atomization and cavitation induced by interactions between focused ultrasound and a water surface, Phys. Fluids **26**, 097105 (2014).

[93] G. Jagadeesh, G. D. Prakash, S. Rakesh, U. S. Allam, M. G. Krishna, S. M. Eswarappa, and D. Chakravortty, Needleless vaccine delivery using micro-shock waves, Clin. Vaccine Immunol. **18**, 539 (2011).

[94] G. I. Taylor, Disintegration of water drops in an electric field, Proc. R. Soc. Lond. A **280**, 383 (1964).

[95] J. F. De La Mora and I. G. Loscertales, The current emitted by highly conducting taylor cones, J. Fluid Mech. **260**, 155 (1994).

[96] A. M. Gañán-Calvo, Generation of Steady Liquid Microthreads and Micron-Sized Monodisperse Sprays in gas Streams, Phys. Rev. Lett. **80**, 285 (1998).

[97] D. DePonte, U. Weierstall, K. Schmidt, J. Warner, D. Starodub, J. Spence, and R. Doak, Gas dynamic virtual nozzle for generation of microscopic droplet streams, J. Phys. D: Appl. Phys. **41**, 195505 (2008).

[98] J. Rosell-Llompart and A. M. Gañán-Calvo, Turbulence in pneumatic flow focusing and flow blurring regimes, Phys. Rev. E **77**, 036321 (2008).

[99] F. Cruz-Mazo, M. O. Wiedorn, M. A. Herrada, S. Bajt, H. N. Chapman, and A. M. Gañán-Calvo, Aerodynamically stabilized taylor cone jets, Phys. Rev. E **100**, 031101(R) (2019).

[100] M. Gamero-Castaño, Dissipation in cone-jet electrosprays and departure from isothermal operation, Phys. Rev. E **99**, 061101(R) (2019).

[101] P. Delrot, M. A. Modestino, F. Gallaire, D. Psaltis, and C. Moser, Inkjet Printing of Viscous Monodisperse Microdroplets by Laser-Induced Flow Focusing, Phys. Rev. Appl. **6**, 024003 (2016).

[102] H. Onuki, Y. Oi, and Y. Tagawa, Microjet Generator for Highly Viscous Fluids, Phys. Rev. Appl. **9**, 014035 (2018).

[103] A. Vogel, J. Noack, K. Nahen, D. Theisen, S. Busch, U. Parlitz, D. Hammer, G. Noojin, B. Rockwell, and R. Birngruber, Energy balance of optical breakdown in water at nanosecond to femtosecond time scales, Appl. Phys. B **68**, 271 (1999).

[104] A. L. Klein, D. Kurilovich, H. Lhuissier, O. O. Versolato, D. Lohse, E. Villermaux, and H. Gelderblom, Drop fragmentation by laser-pulse impact, J. Fluid Mech. **893**, A7 (2020).